A thermo-hydro-mechanical coupled model in local thermal non-equilibrium for fractured HDR reservoir with double porosity

Rachel Gelet, Benjamin Loret, Nasser Khalili

A thermo-hydro-mechanical coupled model in local thermal non-equilibrium for fractured HDR reservoir

Rachel Gelet[a,b], Benjamin Loret[a,*], Nasser Khalili[b]

[a] *Laboratoire Sols, Solides, Structures, B.P. 53X, 38041 Grenoble Cedex, France*
[b] *School of Civil and Environmental Engineering, The University of New South Wales, Sydney 2052, Australia.*

Abstract

The constitutive thermo-hydro-mechanical equations of fractured media are embodied in the theory of mixtures applied to three-phase poroelastic media. The solid skeleton contains two distinct cavities filled with the same fluid. Each of the three phases is endowed with its own temperature. The thermo-mechanical constitutive equations, and the constitutive relations governing generalized diffusion and transfer are structured by, and satisfy, the dissipation inequality. The cavities exchange both mass and energy. Mass exchanges are driven by the jump in scaled chemical potential, and energy exchanges by the jump in coldness. The finite element approximation of the governing equations uses the displacement vector, the two fluid pressures and the three temperatures as primary variables. It is applied to the analysis of a generic hot dry rock (HDR) geothermal reservoir. Three parameters of the model are calibrated from the thermal outputs of the Fenton Hill and Rosemanowes HDR reservoirs. The solid-to-fracture fluid heat transfer coefficient κ_{sf}, which controls the rate of heat exchange between the porous blocks and the fracture fluid, is found in the range 35 to 120 $\mathrm{mW/m^3.K}$. The calibrated model is next applied to simulate circulation tests at the Fenton Hill HDR reservoir. The finer thermo-hydro-mechanical response provided by the dual porosity model with respect to a single porosity model is highlighted in a parameter analysis. Emphasis is put on the influence of the fracture spacing on the effective stress response and on the permeation of the fluid into the porous blocks. The dual porosity model yields a thermally induced effective stress that is less tensile compared with the single porosity response, reflecting distinct pore pressure contributions. This effect becomes significant for large fracture spacings. In agreement with field data, fluid loss is observed to be high initially and to decrease with time.

Keywords: enhanced geothermal system, thermo-hydro-mechanical couplings, dual porosity, mass exchange, heat exchange, fluid loss

1. Introduction

Geothermal energy resources initially tested at Los Alamos National Laboratory, Murphy et al. [1981], continue to attract a significant amount of attention in present-day commercial prototypes, Tenzer [2001]. The development of constitutive models for energy extraction from artificially fractured hot dry rock (HDR) reservoirs requires three main ingredients: (1) a proper thermo-hydro-mechanical coupled model developed from a rational thermodynamics framework; (2) a theory of mixtures for a solid skeleton and one (or several) fluid(s), and (3) local thermal non-equilibrium (LTNE).

The purpose of this work is to contribute to a framework of understanding of the thermo-hydro-mechanical response of fractured media, where, at each geometrical point, the solid skeleton displays two fluid cavities and the temperatures of the solid and fluids are independent. Field observations of pressure buildup and depletion history of reservoirs have demonstrated that standard poro-elasticity may be too crude for modelling purpose.

*Principal corresponding author

Email addresses: rachel.gelet@gmail.com (Rachel Gelet), benjamin.loret@hmg.inpg.fr (Benjamin Loret), n.khalili@unsw.edu.au (Nasser Khalili)

A more elaborate formulation, such as the dual porosity concept, is needed to provide a reliable description of the effective stress and of the fluid pressures in fractured reservoirs, Warren and Root [1963], Kazemi [1969], Zhang and Roegiers [2005].

As for geothermal energy applications, focus so far has been on partially coupled systems in an effort to implement a network of discrete discontinuities, DuTeaux et al. [1996], Bruel [2002], to couple free and forced convection, Bataillé et al. [2006], or to characterize joint closure with a stress dependent law, Kohl et al. [1995]. The closed form solutions by Ghassemi et al. [2005] of the thermally induced stress, in geothermal reservoirs where heat transport is dominated by convection in the fluid phase and by conduction in the solid phase, are worth notice. Still, the influence of a second porosity, which is not participating to forced convection owing to its low permeability, has been systematically disregarded.

Indeed, in spite of their importance in the fields of petroleum engineering, reservoir engineering and geothermal energy extraction, as stressed by e.g. Hayashi et al. [1999], thermo-hydro-mechanical coupling effects in media with double porosity have rarely been investigated, Bai and Roegiers [1994], Bower and Zyvoloski [1997], Masters et al. [2000], Khalili [2003], Nair et al. [2004]. Crucially, the extension of the effective stress concept to media with multiple porosity, and cavities saturated either by fluids or gases, has been an open question for a while. Two propositions remain today: (1) the double effective stress concept, Elsworth and Bai [1992], and (2) the extension of Biot's relationship to dual porosity, Khalili and Valliappan [1996]. Hydro-mechanical dual porosity models, based on the double effective stress concept, have been extended to account for thermal effects, Bai and Roegiers [1994], Bower and Zyvoloski [1997], Masters et al. [2000], Nair et al. [2004]. On the other hand, Khalili and Selvadurai [2003] presented a thermo-hydro-mechanical model for elastic media with double porosity, using a systematic macroscopic approach based on a single effective stress concept. This model, assuming local thermal equilibrium (LTE), has been applied to wellbore stability in the context of enhanced heavy-oil recovery by hot water injection, Gelet et al. [2011]. The importance of an appropriate definition of the effective stress is illustrated in the thermo-hydro-mechanical formulations developed for unsaturated porous media, Loret and Khalili [2000]ab, Khalili and Loret [2001].

A key factor in geothermal energy recovery is the difference in the characteristic times between diffusion of heat in the porous blocks and forced convection in the fracture network, a feature that motivates an analysis that allows for local thermal non-equilibrium. In fact, Gelet et al. [2011] show that continuum models displaying a single porosity can adequately predict the thermal depletion of hot dry rock reservoirs if LTNE between the solid skeleton and the fluid is accounted for. Still, to the exception of the above work, none of the constitutive models accounting for LTNE in mixtures including a solid and a fluid, namely Bowen and Garcia [1970], Pecker and Deresiewicz [1973], Aifantis [1980]ab, De La Cruz and Spanos [1989], Hsu [1999], has targeted geothermal reservoirs. Mechanical engineering applications have addressed packed beds, Minkowycz et al. [1999], Nield et al. [2002]. Quantifying the inter-phase heat transfer coefficient is essentially an open question in the domain of deformable saturated dual porosity media.

Of crucial importance to the economical viability of enhanced geothermal systems is the knowledge of the induced thermal stresses and of the permeation losses into the porous matrix, Armstead and Tester [1987]. Provided that the injection and production wells are appropriately connected, water loss is mainly attributed to the uncontrolled thermal contraction of the rock. According to Richards et al. [1994], water loss may occur according to three mechanisms: steady state diffusive loss, transient loss into storage and loss due to reservoir growth (propagation of the fracture network). To the exceptions of Zyvoloski et al. [1981], Tenma et al. [2008], Ghassemi et al. [2008], few studies really address fluid losses into the matrix, permeation being usually imposed by a continuous leak-off into the formation. In contrast, the present approach quantifies the contributions of the two fluid pressures on the thermally induced effective stress and identifies a mechanism of fluid loss.

A fully coupled finite element formulation for a thermo-elastic fractured medium in local thermal non-equilibrium is exposed here. The fractured medium is described as a dual porosity mixture composed of a solid phase and two fluid phases. While Gelet et al. [2011] consider a single porosity model with one pore pressure and two temperatures, the dual porosity model displays two pore pressures and three temperatures. The solid phase has a special role as it provides the matrix skeleton and encloses the fluid phases in the porous blocks and the fracture network. The three phase model is embedded within a rational thermodynamic framework. The balance equations and the Clausius-Duhem inequality are presented in Sect. 2. Even if the mixture is in LTNE, a single Clausius-Duhem inequality is required for the whole mixture. Three types of contributions, each with its own physical interpretation, are identified in the dissipation (Sect. 3). The

resulting three inequalities motivate the form and structure of the constitutive equations, namely (1) the thermo-mechanical equations linking generalized stresses to generalized strains; (2) the constitutive equations for mass and energy transfers (exchanges) and (3) the constitutive equations for generalized diffusion. The weak form of the field equations, the spatial discretization and time integration procedures to solve the coupled equations through a finite element procedure are summarized in Sect. 5. The primary variables are the displacements, the two pressures of the fluids, the three temperatures of the solid and of the fluid phases. The resulting system of equations is used to address a generic HDR reservoir subjected to the injection of a cool fluid and tested for various fracture spacings (Sect. 6). Comparisons between field data and the simulated response are used to calibrate three parameters of the model so as to match the thermal output (Sect. 7). Particular attention is laid on the magnitude of the specific solid-to-fracture fluid heat transfer coefficient. Once calibrated, the model is used to simulate circulation tests, and the reservoir response is examined in terms of the effective stress and of the permeation of fluid through the porous blocks (Sect. 8). A parametric analysis is performed to explore the response of the model, with special emphasis on the fracture spacing.

Compact or index tensor notation is used throughout. Vector and tensor quantities are identified by bold face letters, e.g. the total stress is denoted $\boldsymbol{\sigma}$, and $\mathbf{I}$ represents the second order identity tensor. $\mathrm{tr}\,(\cdot)$ denotes the trace of a second order tensor, $\nabla(\cdot)$ the gradient operator and $\mathrm{div}\,(\cdot)$ the divergence operator. The subscripts s, p, f refer to the solid skeleton, the pore fluid and the fracture fluid, respectively. Unless stated otherwise, the convention of summation over repeated indices is *not* used.

2. Balance equations for the three phase mixture

Each of the three phases is endowed with its own kinematics, mass and energy content. Accordingly, the thermo-hydro-mechanical response of the mixture requires the partial differential equations in space and time expressing the balances of momentum, the balances of mass and the balances of energy to be satisfied pointwise.

2.1. Basic definitions

Dual porous media are made of three phases, a solid, a fluid in the pores and a fluid in the fractures. Although the fluids are identical, typically water, the two fluid phases are segregated by their spatial location and are therefore viewed as separate constituents endowed with their own independent pressures and temperatures. In the context of the theory of mixtures, the three phases are viewed as three independent overlapping continua. Furthermore, the solid phase, also referred to as the solid skeleton, has a special role as it serves as a reference, Biot [1977]. Each phase contains a single constituent, or species, and therefore the two terms could be used interchangeably. However, the term *constituent* will be used to refer to the individual properties of a species while the term *phase* refers to its contribution to the mixture.

At each point of each phase are defined intrinsic quantities, labeled by subscripts, and apparent or partial quantities, labeled by superscripts. At each point of the fractured porous medium of volume V, the phase k is introduced along with its intrinsic properties of mass M_k and volume V_k. The volumes V_k of the phases sum up to the total volume $V = V_s + V_p + V_f$ of the mixture. The set of all phases is noted by $\mathcal{K} = \{s, p, f\}$ while $\mathcal{K}^* = \{p, f\}$ refers to the set of species which diffuse through the solid skeleton. Each phase k is endowed with a volume fraction n^k, an *intrinsic* density ρ_k, a *partial* density ρ^k,

$$n^k = \frac{V_k}{V}; \qquad \rho_k = \frac{M_k}{V_k}; \qquad \rho^k = \frac{M_k}{V} = n^k \rho_k, \quad k \in \mathcal{K}, \tag{1}$$

and an absolute velocity $\mathbf{v}_k$. The volume fractions sum up to one, $n^s + n^p + n^f = 1$. The total mass density of the mixture ρ is the sum of the apparent contributions,

$$\rho = \sum_{k \in \mathcal{K}} \rho^k \,. \tag{2}$$

At the reference time $t = 0$, the total volume V is denoted V^0. The volume content and the mass content of the fluid phase k per unit reference volume of porous medium are denoted by v^k and m^k, respectively,

$$v^k = \frac{V_k}{V^0} = n^k \frac{V}{V^0}, \qquad m^k = \frac{M_k}{V^0} = \rho_k \, v^k = \rho^k \frac{V}{V^0}, \quad k \in \mathcal{K} \,. \tag{3}$$

The reference and current volumes, V^0 and V respectively, are related by the determinant of the deformation gradient $\mathbf{F}$, which linearizes to $1 + \operatorname{tr}\boldsymbol{\epsilon}$ for small strains,

$$\frac{V}{V^0} = \det \mathbf{F} \sim 1 + \operatorname{tr}\boldsymbol{\epsilon}\,. \tag{4}$$

The mass flux $\mathbf{M}_k$ and the volume flux $\mathbf{J}_k$ per unit current area of the mixture measure the relative velocity of the fluid phase k with respect to the solid,

$$\mathbf{M}_k = \rho_k\,\mathbf{J}_k = \rho^k\,(\mathbf{v}_k - \mathbf{v}_s)\,, \quad k \in \mathcal{K}^*\,. \tag{5}$$

The solid phase is endowed with its own (infinitesimal) strain tensor $\boldsymbol{\epsilon} = \frac{1}{2}\left(\nabla\mathbf{u} + (\nabla\mathbf{u})^{\mathrm{T}}\right)$, which is defined from the macroscopic displacement vector $\mathbf{u}$ and which is constitutively decomposed into an elastic contribution $\boldsymbol{\epsilon}^{\mathrm{el}}$ and a thermal contribution $\boldsymbol{\epsilon}^{\theta}$,

$$\boldsymbol{\epsilon} = \boldsymbol{\epsilon}^{\mathrm{el}} + \boldsymbol{\epsilon}^{\theta}\,. \tag{6}$$

The partial stress and pressures of the three phases, $\boldsymbol{\sigma}^s$ and pressures p^k, which are linked to the intrinsic stress $\boldsymbol{\sigma}_s$ and pressures p_k of the associated phases through the volume fractions,

$$\boldsymbol{\sigma}^s = n^s\boldsymbol{\sigma}_s, \quad \boldsymbol{\sigma}^k = -n^k p_k\,\mathbf{I}, \quad k \in \mathcal{K}^*\,, \tag{7}$$

sum up to the total stress,

$$\boldsymbol{\sigma} = \boldsymbol{\sigma}^s + \boldsymbol{\sigma}^p + \boldsymbol{\sigma}^f\,. \tag{8}$$

The total stress $\boldsymbol{\sigma}$ and the effective stress $\bar{\boldsymbol{\sigma}}$ may be decomposed into a spherical part and a deviatoric part $\mathbf{s}$, by use of the mean stresses $p = -\frac{1}{3}\operatorname{tr}\boldsymbol{\sigma}$ and $\bar{p} = -\frac{1}{3}\operatorname{tr}\bar{\boldsymbol{\sigma}}$,

$$\boldsymbol{\sigma} = -p\,\mathbf{I} + \mathbf{s}, \qquad \bar{\boldsymbol{\sigma}} = -\bar{p}\,\mathbf{I} + \mathbf{s}. \tag{9}$$

The stress components are positive in tension so that the mean stresses p and $\bar{p}$ are counted positive in compression. The elastic strain $\boldsymbol{\epsilon}^{\mathrm{el}} = \mathbf{C}^{\mathrm{DS}}\,\bar{\boldsymbol{\sigma}}$ is by definition linked by a one-to-one relationship with the effective stress $\bar{\boldsymbol{\sigma}}$ through the drained compliance tensor $\mathbf{C}^{\mathrm{DS}}$. In an isotropic context,

$$\operatorname{tr}\boldsymbol{\epsilon}^{\mathrm{el}} = -c^{\mathrm{DS}}\,\bar{p}, \quad \mathbf{e}^{\mathrm{el}} = \frac{\mathbf{s}}{2\,\mu^{\mathrm{DS}}}\,, \tag{10}$$

in which c^{DS} is the drained compressibility of the solid skeleton and μ^{DS} its shear modulus. $\mathbf{e}^{\mathrm{el}}$ denotes the deviatoric part of the elastic strain $\boldsymbol{\epsilon}^{\mathrm{el}} = \frac{1}{3}\operatorname{tr}\boldsymbol{\epsilon}^{\mathrm{el}}\,\mathbf{I} + \mathbf{e}^{\mathrm{el}}$. In this isotropic context, the deviatoric parts of the elastic and total strains, $\mathbf{e}^{\mathrm{el}}$ and $\mathbf{e}$ respectively, are equal.

Furthermore, the thermodynamical state of each fluid constituent is measured by its pressure p_k, its temperature T_k, its entropy S_k and thermodynamic potentials per unit current mass of the constituent such as the internal energy U_k, the free energy E_k, the enthalpy H_k, and the chemical potential G_k, also called free enthalpy,

$$E_k = U_k - T_k\,S_k, \quad H_k = U_k + \frac{p_k}{\rho_k}, \quad G_k = H_k - T_k\,S_k, \quad k \in \mathcal{K}^*\,. \tag{11}$$

Thermodynamic potentials per unit current volume are denoted by a lower letter, e.g. $e^k = \rho^k E_k$ for the free energy and $s^k = \rho^k S_k$ for the entropy.

2.2. Balances of momentum, mass and energy

A single balance of momentum is required for the mixture as a whole,

$$\operatorname{div}\boldsymbol{\sigma} + \rho\,\mathbf{b} = \mathbf{0}\,, \tag{12}$$

the body force $\rho\,\mathbf{b} = \sum_{k\in\mathcal{K}}\rho^k\,\mathbf{b}_k$ being contributed additively by the constituents. Since the mass of the solid constituent is constant, a balance of mass is required for the fluid phases only,

$$\operatorname{div}\mathbf{J}_k + f_k = 0, \quad f_k \equiv n^k\frac{1}{\rho_k}\frac{\mathrm{d}\rho_k}{\mathrm{d}t} + \frac{1}{V}\frac{\mathrm{d}V_k}{\mathrm{d}t} - \frac{\hat{\rho}^k}{\rho_k}, \quad k \in \mathcal{K}^*\,. \tag{13}$$

Mass conservation implies the rates of mass change $\hat{\rho}^k$ to sum up to zero,

$$\sum_{k\in\mathcal{K}^*} \hat{\rho}^k = 0, \qquad \hat{\rho}^f = -\hat{\rho}^p \,. \tag{14}$$

This study aims to describe the transient period, referred to as local thermal non-equilibrium (LTNE), before the system reaches local thermal equilibrium (LTE). Hence, a balance of energy is required for each phase. Besides terms which are standard for single phases, the energy equations display terms that embody the rates of energy exchanges $\hat{e}^k$, $k \in \mathcal{K}$. The balance of energy for the solid phase accounts for the flux of thermal energy due to conduction $\mathbf{q}_s$, the rate of solid entropy and the rate of energy exchange between the solid phase and the other phases,

$$\text{div } \mathbf{q}_s + \mathcal{L}_s = 0, \quad \mathcal{L}_s \equiv T_s \frac{\mathrm{d}s^s}{\mathrm{d}t} + \hat{e}^s \,. \tag{15}$$

The balance of energy for the fluid phase k accounts for the flux of thermal energy due to conduction $\mathbf{q}_k$, the rate of fluid entropy, the rates in free energy due to mass transfer and forced convection, and the transfer of energy between the fluid phase k and the other phases,

$$\text{div } \mathbf{q}_k + \mathcal{L}_k = 0, \quad \mathcal{L}_k \equiv T_k \frac{\mathrm{d}s^k}{\mathrm{d}t} + \hat{\rho}^k H_k + \mathbf{M}_k \cdot \nabla H_k + \hat{e}^k, \quad k \in \mathcal{K}^* \,. \tag{16}$$

Energy conservation implies the rates of energy transfer $\hat{e}^k$ to sum up to zero,

$$\sum_{k\in\mathcal{K}} \hat{e}^k = 0, \qquad \hat{e}^s = -\hat{e}^p - \hat{e}^f \,. \tag{17}$$

2.3. The Clausius-Duhem inequality

A single dissipation inequality is required at the mixture level. The dissipation associated with each phase is obtained by inserting the balance of energy into the balance of entropy of each species. The entropy productions of the phases are next summed *without* multiplying by the phase temperatures. The resulting inequality, referred to as Clausius-Duhem inequality, proves a useful guide to restrict the form of the constitutive couplings, Eringen and Ingram [1965], Bowen and Garcia [1970]. The Clausius-Duhem inequality may be advantageously rewritten in a form that highlights the thermo-mechanical, transfer and diffusion contributions, $\mathrm{d}D = \mathrm{d}D_1 + \mathrm{d}D_2 + \mathrm{d}D_3 \geq 0$, namely,

$$\begin{aligned}
\frac{\mathrm{d}D_1}{\mathrm{d}t} &= \sum_{k\in\mathcal{K}} \frac{1}{T_k} \left(-\frac{\mathrm{d}e^k}{\mathrm{d}t} + \left(\boldsymbol{\sigma}^k - e^k\,\mathbf{I}\right) : \nabla \mathbf{v}_s - s^k \frac{\mathrm{d}T_k}{\mathrm{d}t} \right) + \sum_{k\in\mathcal{K}^*} \frac{1}{\det\mathbf{F}} \frac{G_k}{T_k} \frac{\mathrm{d}m^k}{\mathrm{d}t} \geq 0, \\
\frac{\mathrm{d}D_2}{\mathrm{d}t} &= -\sum_{k\in\mathcal{K}^*} \left(G_k + \frac{1}{2}\left(\mathbf{v}_k - \mathbf{v}_s\right)^2 - \frac{1}{2}\mathbf{v}_s^2 \right) \frac{1}{T_k}\, \hat{\rho}^k - \sum_{k\in\mathcal{K}} \hat{e}^k_{\mathcal{S}} + \sum_{k\in\mathcal{K}} \frac{1}{T_k} \hat{e}^k \geq 0, \\
\frac{\mathrm{d}D_3}{\mathrm{d}t} &= -\sum_{k\in\mathcal{K}^*} \mathbf{J}_k \cdot \frac{1}{T_k} \left(\nabla p_k + \rho_k \big(\frac{\mathrm{d}^k \mathbf{v}_k}{\mathrm{d}t} - \mathbf{b}_k \big) \right) - \sum_{k\in\mathcal{K}} \mathbf{q}_k \cdot \frac{\nabla T_k}{T_k^2} \geq 0 \,,
\end{aligned} \tag{18}$$

which are required to be positive individually, Loret [2008], Gelet [2011]. Note that the rate of entropy exchange between phase k and the other phases of the mixture $\hat{e}^k_{\mathcal{S}}$ appears to have no work conjugate variable. The mixture has been assumed to be closed with respect to momentum, eq (12), to mass, eq (14), and to energy, eq (17). Similarly, it is assumed to be closed with respect to entropy, so that the sum of the rates of entropy transfer vanish,

$$\sum_{k\in\mathcal{K}} \hat{e}^k_{\mathcal{S}} = 0 \,. \tag{19}$$

Therefore the constitutive equations of individual rates of entropy transfer are not needed here. On the other hand, constitutive equations need to be developed for the rates of mass transfer $\hat{\rho}^k$ and the rates of energy transfer $\hat{e}^k$. Although not made explicit here, the momentum transfer of individual phases could also be retrieved from Darcy's law.

The set of independent variables used so far has tacitly included the strain, the pressures and the temperatures. Alternatively, the total stress might be substituted to the strain as an independent variable. The modification is realized by performing a partial Legendre transform of the elastic potential of the mixture $\Psi(\boldsymbol{\epsilon}, p_p, p_f, T_s, T_p, T_f) = m^s\, E_s - \sum_{k\in\mathcal{K}^*} v^k p_k$ that yields the complementary potential Ψ_c,

$$\Psi_c(\boldsymbol{\sigma}, p_p, p_f, T_s, T_p, T_f) = \Psi(\boldsymbol{\epsilon}, p_p, p_f, T_s, T_p, T_f) - \det\mathbf{F}\,\boldsymbol{\sigma} : \boldsymbol{\epsilon}\,. \tag{20}$$

A reference configuration is identified, in which the temperatures of the three phases are equal. Departure from this reference state is denoted by the symbol $\Delta(\cdot)$.

The Clausius-Duhem inequality is linearized by (1) neglecting the inertial terms in the transfer contributions $\mathrm{d}D_2$ and in the diffusion contributions $\mathrm{d}D_3$; (2) identifying the current and reference configurations so that $\det\mathbf{F}$ may be set to 1. Within an updated Lagrangian analysis, the volume content v^k and the volume fraction n^k are equal at each time, but their rates differ, namely $\mathrm{d}v^k = \mathrm{d}n^k + n^k\,\mathrm{tr}\,\boldsymbol{\epsilon}$. The same remark applies to the mass content m^k and apparent mass density ρ^k. The thermo-mechanical contribution to the Clausius-Duhem inequality $\mathrm{d}D_1$, eqn $(18)_1$, is modified by multiplying by the temperature of the solid constituent T_s,

$$\begin{aligned}
T_s\,\frac{\mathrm{d}D_1}{\mathrm{d}t} &= -\frac{\mathrm{d}\Psi_c}{\mathrm{d}t} - \frac{\mathrm{d}\boldsymbol{\sigma}}{\mathrm{d}t} : \boldsymbol{\epsilon} - s^s\frac{\mathrm{d}T_s}{\mathrm{d}t} - \sum_{k\in\mathcal{K}^*} v^k\frac{\mathrm{d}p_k}{\mathrm{d}t} \geq 0,\\
\frac{\mathrm{d}D_2}{\mathrm{d}t} &= -\sum_{k\in\mathcal{K}^*}\frac{G_k}{T_k}\,\hat{\rho}^k + \sum_{k\in\mathcal{K}}\frac{1}{T_k}\hat{e}^k \geq 0,\\
\frac{\mathrm{d}D_3}{\mathrm{d}t} &= -\sum_{k\in\mathcal{K}^*}\mathbf{J}_k\cdot\frac{\nabla p_k}{T_k} - \sum_{k\in\mathcal{K}}\mathbf{q}_k\cdot\frac{\nabla T_k}{T_k^2} \geq 0\,.
\end{aligned} \tag{21}$$

Thermo-mechanical constitutive assumptions and simplifications are motivated in the next section.

3. Constitutive equations

The Clausius-Duhem inequalities (21) serve as guidelines to develop the constitutive equations:

(1) the thermo-mechanical behavior is constructed in order the thermo-mechanical term $\mathrm{d}D_1$ to *exactly vanish*, Sect. 3.1. The thermo-mechanical behavior of a single fluid k is introduced separately from the thermo-mechanical elastic equations, Sect. 3.2;

(2) the energy dissipation is due exclusively to the transfers of mass and energy between phases, to diffusion of fluids through the solid skeleton and to conduction and convection of heat;

(3) the constitutive equations of mass and energy exchanges are expressed in a format that ensures the second term $\mathrm{d}D_2$ to be positive, Sect. 3.3;

(4) the constitutive equations of thermal and hydraulic diffusions enforce the third term $\mathrm{d}D_3$ to be positive as well, Sect. 3.4.

3.1. Thermo-mechanical elastic equations

At constant total stress and pore pressures, the sole change of solid temperature leads to a volume change of the solid skeleton, the strain is uniform over the phases, and the volume change of each of the three phases is proportional to its volume fraction, Loret and Khalili [2000]a. Therefore the complementary energy depends on the restricted set of variables $\{\boldsymbol{\sigma}, p_p, p_f, T_s\}$. Then, the vanishing of $\mathrm{d}D_1$ implies that the complementary energy $\Psi_c(\boldsymbol{\sigma}, p_p, p_f, T_s)$ can be used as a thermo-elastic potential, that delivers the work conjugate variables $\{\boldsymbol{\epsilon}, v^p, v^f, s^s\}$,

$$\boldsymbol{\epsilon} = -\frac{\partial\Psi_c}{\partial\boldsymbol{\sigma}}; \qquad -v^k = \frac{\partial\Psi_c}{\partial p_k}, \quad k\in\mathcal{K}^*; \qquad -s^s = \frac{\partial\Psi_c}{\partial T_s}\,. \tag{22}$$

The complementary energy is assumed to be an isotropic quadratic function of the stress, and the sum of a quadratic function and of an affine function of the pressures and solid temperature,

$$\begin{aligned}\Psi_c(\boldsymbol{\sigma}, p_p, p_f, T_s) = &-\frac{1}{2}\left(c_{ss}\, p^2 + c_{pp}\, p_p^2 + c_{ff}\, p_f^2 + 2\, c_{sp}\, p\, p_p + 2\, c_{sf}\, p\, p_f + 2\, c_{pf} p_p\, p_f\right) - \frac{|\mathbf{s}|^2}{4\,\mu^{\text{DS}}} \\ &-\frac{1}{2} c_{TT}\, \Delta T_s^2 - \Delta T_s\left(c_{Ts}\, p + c_{Tp}\, p_p + c_{Tf}\, p_f\right) \\ &-\sum_{k\in\mathcal{K}^*} (v^k)^0 p_k - (s^s)^0 T_s\,.\end{aligned} \tag{23}$$

Therefore the deviatoric stress and strain are proportional, and the scalar work conjugate variables $(-p, \operatorname{tr}\boldsymbol{\epsilon})$, (p_p, v^p), (p_f, v^f), and (s^s, T_s) are related by a symmetric and constant matrix,

$$\begin{bmatrix} -\operatorname{tr}\boldsymbol{\epsilon} \\ \Delta v^p \\ \Delta v^f \\ \Delta s^s \end{bmatrix} = \begin{bmatrix} c_{ss} & c_{sp} & c_{sf} & c_{sT} \\ c_{ps} & c_{pp} & c_{pf} & c_{pT} \\ c_{fs} & c_{fp} & c_{ff} & c_{fT} \\ c_{Ts} & c_{Tp} & c_{Tf} & c_{TT} \end{bmatrix} \begin{bmatrix} p \\ p_p \\ p_f \\ \Delta T_s \end{bmatrix}, \quad \mathbf{e} = \frac{\mathbf{s}}{2\mu^{\text{DS}}}\,. \tag{24}$$

The identification of the constitutive coefficients is best addressed *via* the equivalent mixed format,

$$\begin{bmatrix} p \\ \Delta v^p \\ \Delta v^f \\ \Delta s^s \end{bmatrix} = \begin{bmatrix} -1/c & \xi_p & \xi_f & c_T/c^{\text{DS}} \\ \xi_p & c_{22} & c_{23} & (n^p - \xi_p)\, c_T \\ \xi_f & c_{32} & c_{33} & \left(n^f - \xi_f\right) c_T \\ c_T/c^{\text{DS}} & (n^p - \xi_p)\, c_T & \left(n^f - \xi_f\right) c_T & \rho^s\, C_s^{(v)}/T_s \end{bmatrix} \begin{bmatrix} \operatorname{tr}\boldsymbol{\epsilon} \\ p_p \\ p_f \\ \Delta T_s \end{bmatrix}. \tag{25}$$

The thermo-mechanical constitutive relations extend the concept of effective stress, Biot [1941], to dual porosity,

$$\frac{\operatorname{tr}\boldsymbol{\sigma}}{3} + \xi_p p_p + \xi_f p_f = \frac{1}{c^{\text{DS}}}\left(\operatorname{tr}\boldsymbol{\epsilon} - c_T \Delta T_s\right). \tag{26}$$

The effective stress coefficients ξ_p and ξ_f and the other mechanical coefficients have been identified *via* a loading decomposition, Khalili and Valliappan [1996],

$$\begin{aligned} \xi_p &= (c_p - c_s)/c^{\text{DS}}, \\ \xi_f &= 1 - c_p/c^{\text{DS}}, \\ c_{22} &= \left(\xi_f - n^f\right)(c_p - c_s) + c_s\left(\xi_p - n^p\right), \\ c_{33} &= \left(\xi_f - n^f\right)(c_p - c_s) + c_s\left(\xi_f - n^f\right), \\ c_{23} &= c_{32} = -\left(\xi_f - n^f\right)(c_p - c_s)\,. \end{aligned} \tag{27}$$

The relations (25) and (27) use the drained compressibility of the solid skeleton c^{DS} [1/Pa], the compressibility of the porous blocks c_p, the compressibility of the solid grains c_s, the volumetric thermal expansion coefficient of the solid phase c_T [1/K], and the heat capacity of the solid $C_s^{(v)}$ per unit mass of solid, at constant strain and fluid pressures [J/kg.K].

The constitutive equations for the apparent entropies of the fluids are expressed separately from the thermo-mechanical relations (25) in Sect. 3.2.

3.2. Thermo-mechanical properties of the single fluid k

The entropy S_k, the chemical potential G_k and the enthalpy H_k of the fluids enter the balance of energy (16). The variation of the specific volume $v_k = 1/\rho_k$ for a compressible and dilatable fluid k,

$$\frac{\mathrm{d}v_k}{v_k} = c_{kT}\,\mathrm{d}T_k - c_{kH}\,\mathrm{d}p_k, \tag{28}$$

introduces the compressibility c_{kH} [1/Pa] and the thermal expansion coefficient c_{kT} [1/K],

$$c_{kH} = -\frac{1}{v_k}\Big(\frac{\partial v_k}{\partial p_k}\Big)_{|T_k} = \frac{1}{\rho_k}\Big(\frac{\partial \rho_k}{\partial p_k}\Big)_{|T_k}, \qquad c_{kT} = \frac{1}{v_k}\Big(\frac{\partial v_k}{\partial T_k}\Big)_{|p_k} = -\frac{1}{\rho_k}\Big(\frac{\partial \rho_k}{\partial T_k}\Big)_{|p_k}. \tag{29}$$

For constant coefficients c_{kT} and c_{kH}, the specific volume results as a non-linear function of the departures of pressure and temperature from the reference state labeled by a zero superscript,

$$v_k = v_k^0\,\exp\left(-c_{kH}\left(p_k - p_k^0\right) + c_{kT}\left(T_k - T_k^0\right)\right). \tag{30}$$

Moreover, as $(\partial S_k/\partial v_k)_{|T_k} = c_{kT}/c_{kH}$, the differential of the entropy $\mathrm{d}S_k$,

$$T_k\,\mathrm{d}S_k = T_k\frac{c_{kT}}{c_{kH}}\,\mathrm{d}v_k + C_k^{(v)}\,\mathrm{d}T_k\,, \tag{31}$$

integrates to,

$$S_k - S_k^0 = \frac{c_{kT}}{c_{kH}}\,(v_k - v_k^0) + C_k^{(v)}\,\mathrm{Ln}\,\frac{T_k}{T_k^0}\,, \tag{32}$$

the heat capacity at constant volume $C_k^{(v)} = T_k\left(\partial S_k/\partial T_k\right)_{|v_k}$ [J/kg.K] being assumed constant.

The incremental variations of the chemical potential G_k and of the enthalpy H_k express in terms of the specific volume v_k and of the entropy S_k,

$$\mathrm{d}G_k = v_k\mathrm{d}p_k - S_k\mathrm{d}T_k, \quad \mathrm{d}H_k = v_k\mathrm{d}p_k + T_k\mathrm{d}S_k\,, \tag{33}$$

and integrate to,

$$\begin{aligned} G_k - G_k^0 &= -\frac{v_k - v_k^0}{c_{kH}} + \left(C_k^{(v)} + \frac{c_{kT}}{\rho_k c_{kH}} - S_k^0\right)\left(T_k - T_k^0\right) - C_k^{(v)}\,T_k\,\mathrm{Ln}\,\frac{T_k}{T_k^0}, \\ H_k - H_k^0 &= -\frac{v_k - v_k^0}{c_{kH}}(1 - T_k\,c_{kT}) + \left(C_k^{(v)} + \frac{c_{kT}}{\rho_k c_{kH}}\right)\left(T_k - T_k^0\right). \end{aligned} \tag{34}$$

In spite of the third law of thermodynamics, Kestin [1966], the reference potentials G_k^0, H_k^0 and S_k^0 are conventional, and need to be assigned.

The enthalpy may alternatively be expressed as a function of pressure and temperature,

$$\mathrm{d}H_k = v_k(1 - T_k c_{kT})\,\mathrm{d}p_k + C_k^{(p)}\,\mathrm{d}T_k\,, \tag{35}$$

through the heat capacity at constant pressure $C_k^{(p)}$ [J/kg.K],

$$C_k^{(p)} = C_k^{(v)} + \frac{T_k c_{kT}^2}{\rho_k c_{kH}}\,. \tag{36}$$

Note that the differential operator d appearing in the relations above is arbitrary, i.e. it may refer to time or space.

3.3. Constitutive equations for mass and heat transfers

The constitutive equations of mass and energy exchanges are defined by enforcing the second term of the Clausius-Duhem inequality $\mathrm{d}D_2$ to be positive, eqn (21). For that purpose, the rate of mass exchange $\hat{\rho}^k$ and the rate of energy exchange $\hat{e}^k$ are viewed as work-conjugated respectively to the chemical potential scaled by the temperature $-G_k/T_k$ and to the coldness (inverse temperature) $1/T_k$. Due to a lack of *in situ* measurements and as a first approximation, no coupling is assumed between mass transfer and energy transfer. In other words, the transfer counterparts of the thermo-osmosis and of the isothermal heat transfer in the diffusion constitutive equations developed in Section 3.4 are not introduced.

The transfers satisfy the closure relations (14) and (17) so that a single mass rate, e.g. the rate $\hat{\rho}^p$ of the pore fluid, and two rates of energy exchange, e.g. the rates $\hat{e}^p$ and $\hat{e}^f$ associated with the fluids, are needed. Consequently, equation (21) may be rearranged to highlight the driving forces of the transfer mechanisms, namely the jumps in scaled chemical potential $-G_k/T_k$ across the fluid phases and in coldness $1/T_k$ across the three phases,

$$\begin{aligned} &\text{mass transfer :} \quad -\hat{\rho}^p \left(\frac{G_p}{T_p} - \frac{G_f}{T_f}\right) \geq 0\,; \\ &\text{heat transfer :} \quad -\hat{e}^p \left(\frac{1}{T_p} - \frac{1}{T_s}\right) - \hat{e}^f \left(\frac{1}{T_f} - \frac{1}{T_s}\right) \geq 0\,. \end{aligned} \tag{37}$$

The first inequality is satisfied by setting

$$\hat{\rho}^p = -\eta\, \rho_p^2\, T_p^0 \left(\frac{G_p}{T_p} - \frac{G_f}{T_f}\right) = -\hat{\rho}^f\,. \tag{38}$$

This constitutive equation for mass transfer extends the existing isothermal formulation where the mass transfer is controlled by the difference of pressures between the cavities. The actual leakage parameter η is defined in Sect. 6.3. The dissipation inequality $(37)_1$ is clearly satisfied for $\eta \geq 0$.

The constitutive relations of energy transfer assume the simple linear format,

$$\begin{aligned} \hat{e}^s &= \kappa_{sp}(T_s - T_p) + \kappa_{sf}(T_s - T_f), \\ \hat{e}^p &= \kappa_{sp}(T_p - T_s) + \kappa_{pf}(T_p - T_f), \\ \hat{e}^f &= \kappa_{sf}(T_f - T_s) + \kappa_{pf}(T_f - T_p)\,. \end{aligned} \tag{39}$$

These relations retrieve the proposition of Bowen and Chen [1975] for porous media with a single porosity. The coefficients κ_{ab}, $ab = sp, sf, pf$, are the *volumetric* or *specific* inter-phase heat transfer coefficients [W/m^3.K]. The second inequality, in eqn (37), can be written as a sum of terms $\kappa_{ab}(T_a - T_b)^2/(T_a T_b)$ over $ab = sp, sf, pf$, so that the inequality is satisfied if the three *specific* inter-phase heat transfer coefficients are positive, namely $\kappa_{sp} \geq 0$, $\kappa_{sf} \geq 0$ and $\kappa_{pf} \geq 0$.

3.4. Constitutive equations for hydraulic and heat diffusions

The diffusion constitutive equations are similarly defined by enforcing the third term of the Clausius-Duhem inequality $\mathrm{d}D_3$ to be positive. The volume flux $\mathbf{J}_k$ is seen as work-conjugated to the hydraulic gradient $-\nabla p_k/T_k$ and the heat flux $\mathbf{q}_k$ is conjugated to the thermal gradient $\nabla(1/T_k)$. Since the fluids are segregated by their spatial location, no coupling between the pore fluid diffusion and the fracture fluid diffusion is physically appropriate. For each fluid k, the *extended Darcy's law* equation describing hydraulic diffusion under combined hydraulic and thermal gradients assumes the coupled format,

$$\mathbf{J}_k = -T_k\, \frac{k_k}{\mu_k} \cdot \left(\frac{\nabla p_k}{T_k}\right) - n^k\, T_k^2\, \Theta_k \left(\frac{\nabla T_k}{T_k^2}\right), \quad k \in \mathcal{K}^*\,, \tag{40}$$

where k_k is the intrinsic permeability [m^2], μ_k is the dynamic viscosity of the fluid [Pa.s] and Θ_k the thermo-osmosis coupling coefficient $\left[\mathrm{m}^2/\mathrm{s.K}\right]$.

Similarly, the *extended Fourier's law* defining the heat fluxes $\mathbf{q}_k$, $k \in \mathcal{K}$, under combined hydraulic and thermal gradients displays no coupling over phases, but *a priori* it includes an internal thermo-hydraulic coupling,

$$\begin{aligned} \mathbf{q}_s &= -n^s\, T_s^2\, \Lambda_s \left(\frac{\nabla T_s}{T_s^2}\right), \\ \mathbf{q}_k &= -n^k\, T_k^2\, \Phi_k \left(\frac{\nabla p_k}{T_k}\right) - n^k\, T_k^2\, \Lambda_k \left(\frac{\nabla T_k}{T_k^2}\right), \quad k \in \mathcal{K}^* . \end{aligned} \tag{41}$$

The Φ_k's are called the isothermal heat flow coefficients $\left[\mathrm{m}^2/\mathrm{s.K}\right]$, and the Λ_k's are the thermal conductivities [W/m.K]. Along Onsager's reciprocity principle, the generalized diffusion matrix linking the vector of fluxes $\{\mathbf{J}_p,\, \mathbf{J}_f,\, \mathbf{q}_s,\, \mathbf{q}_p,\, \mathbf{q}_f\}$ to the driving gradients $\{-\nabla p_p/T_p,\, -\nabla p_f/T_f,\, -\nabla T_s/T_s^2,\, -\nabla T_p/T_p^2,\, -\nabla T_f/T_f^2\}$ is assumed symmetric so that the thermo-osmosis coefficients are equal to the isothermal heat flux coefficients: $\Theta_k = \Phi_k$, $k \in \mathcal{K}^*$. The Clausius-Duhem inequality $(21)_3$ is satisfied if the generalized diffusion matrix is positive semi-definite, which is ensured by the inequalities,

$$\Lambda_k \geq 0, \quad k \in \mathcal{K}; \qquad \frac{k_k}{\mu_k} \geq 0, \quad k \in \mathcal{K}^*; \qquad \Lambda_k \frac{k_k}{\mu_k} - n^k T_k \Theta_k^2 \geq 0, \quad k \in \mathcal{K}^* . \tag{42}$$

4. The coupled field equations

Inserting the thermo-mechanical constitutive equations (6) and $(25)_1$ into the balance of momentum (12) yields three coupled partial differential equations for the displacement vector, the pressures and the solid temperature,

$$\mu^{\mathrm{DS}}\, \nabla^2 \mathbf{u} + (\lambda^{\mathrm{DS}} + \mu^{\mathrm{DS}})\, \nabla(\mathrm{div}\, \mathbf{u}) - \xi_p\, \nabla p_p - \xi_f\, \nabla p_f - \frac{c_T}{c^{\mathrm{DS}}}\, \nabla T_s - \rho\, \mathbf{b} = \mathbf{0} . \tag{43}$$

The drained compressibility of the solid skeleton c^{DS} and the Lamé's constants of the drained solid λ^{DS} and μ^{DS} are deduced from the drained Young's modulus E and Poisson's ratio ν through the standard relationships,

$$c^{\mathrm{DS}} = \frac{3(1-2\nu)}{E}, \quad \lambda^{\mathrm{DS}} = \frac{E\nu}{(1+\nu)(1-2\nu)}, \quad \mu^{\mathrm{DS}} = \frac{E}{2(1+\nu)} . \tag{44}$$

A field equation describing seepage is obtained by inserting the constitutive relations $(25)_2$, $(25)_3$, (28) and (40) into the balance of mass (13), yielding in turn for the pores and for the fractures,

$$\mathrm{div}\left(\frac{k_p}{\mu_p}\, \nabla p_p + n^p \Theta_p\, \nabla T_p\right) = a_{pp}\, \frac{\partial p_p}{\partial t} + a_{pf}\, \frac{\partial p_f}{\partial t} + \xi_p\, \mathrm{div}\, \frac{\partial \mathbf{u}}{\partial t} + a_{pT_s}\, \frac{\partial T_s}{\partial t} + a_{pT_p}\, \frac{\partial T_p}{\partial t} - \frac{\hat{\rho}^p}{\rho_p} , \tag{45}$$

$$\mathrm{div}\left(\frac{k_f}{\mu_f}\, \nabla p_f + n^f \Theta_f\, \nabla T_f\right) = a_{ff}\, \frac{\partial p_f}{\partial t} + a_{pf}\, \frac{\partial p_p}{\partial t} + \xi_f\, \mathrm{div}\, \frac{\partial \mathbf{u}}{\partial t} + a_{fT_s}\, \frac{\partial T_s}{\partial t} + a_{fT_f}\, \frac{\partial T_f}{\partial t} - \frac{\hat{\rho}^f}{\rho_f} , \tag{46}$$

the rates of mass transfer being defined by the non-linear constitutive laws $(34)_1$ and (38).

Heat flow, forced convection and heat transfer in presence of local thermal non-equilibrium are obtained by inserting the constitutive equations $(25)_4$, (35), (31), (41) into the equations of balance of energy (15) and (16), resulting in turn for the solid, pore fluid and fracture fluid to,

$$\begin{aligned} \mathrm{div}\, (n^s \Lambda_s\, \nabla T_s) &= a_{T_sT_s}\, \frac{\partial T_s}{\partial t} + T_s \frac{c_T}{c^{\mathrm{DS}}}\, \mathrm{div}\, \frac{\partial \mathbf{u}}{\partial t} + T_s\, a_{pT_s}\, \frac{\partial p_p}{\partial t} + T_s\, a_{fT_s}\, \frac{\partial p_f}{\partial t} \\ &+ \kappa_{sp}\, (T_s - T_p) + \kappa_{sf}\, (T_s - T_f) , \end{aligned} \tag{47}$$

$$\begin{aligned} \mathrm{div}\, (n^p \Lambda_p\, \nabla T_p + T_p n^p \Theta_p\, \nabla p_p) &= a_{T_pT_p}\, \frac{\partial T_p}{\partial t} + T_p\, a_{pT_p}\, \frac{\partial p_p}{\partial t} \\ &+ \mathbf{M}_p \cdot \left(v_p (1 - T_p c_{pT})\, \nabla p_p + C_p^{(p)}\, \nabla T_p\right) + \hat{\rho}^p\, H_p \\ &+ \kappa_{sp}\, (T_p - T_s) + \kappa_{pf}\, (T_p - T_f) , \end{aligned} \tag{48}$$

$$
\begin{aligned}
\text{div}\,\left(n^f \Lambda_f\,\nabla T_f + T_f n^f \Theta_f\,\nabla p_f\right) &= a_{T_f T_f}\frac{\partial T_f}{\partial t} + T_f\, a_{f T_f}\frac{\partial p_f}{\partial t} \\
&+ \mathbf{M}_f \cdot \left(v_f(1 - T_f c_{fT})\,\nabla p_f + C_f^{(p)}\,\nabla T_f\right) + \hat{\rho}^f\, H_f \\
&+ \kappa_{sf}\,(T_f - T_s) + \kappa_{pf}\,(T_f - T_p)\ .
\end{aligned}
\tag{49}
$$

The enthalpies of the fluids H_p and H_f are defined by eqns $(34)_2$. Note that the term $\hat{\rho}^p\,(H_p - H_f)$ cancels out when the fracture spacing B tends to zero, i.e. when hydraulic and thermal equilibria are recovered. The coefficients appearing in equations (45) to (49) are identified in terms of known properties,

$$
\begin{aligned}
&a_{kk} = n^k\, c_{H,k} + (\xi_k - n^k)\, c_s - a_{pf}, \quad k = p, f; \quad a_{pf} = -(\xi_f - n^f)(c_p - c_s), \\
&a_{kT_s} = (n^k - \xi_k)\, c_T, \quad k = p, f; \quad a_{kT_k} = -n^k\, c_{T,k}, \quad k = p, f; \\
&a_{T_s T_s} = n^s \rho_s\, C_s^{(v)}; \quad a_{T_k T_k} = n^k \rho_k\, C_k^{(p)}, \quad k = p, f\,.
\end{aligned}
\tag{50}
$$

In a HDR reservoir context, if the fractured medium is described with a single porosity model, the fluid in the porous blocks is motionless with respect to the solid. In other words, the pores introduce a residual porosity, isolated from the fracture network. On the other hand, the pores contribute to the diffusion of heat. A comparison with a single porosity model serves to highlight the influence of the dual porosity concept on the overall reservoir response.

The single porosity model is recovered by setting the pore volume fraction n^p to zero, which implies $c_p = c_s$. Consequently, $\xi_p = 0$ and $\xi_f = 1 - c_s/c^{\mathrm{DS}}$, and Biot's effective stress is recovered. Details pertaining to the single porosity model are postponed to Appendix A.

5. Finite element discretization

The finite element formulation is developed for the following primary unknowns: displacement vector $\mathbf{u}$, pressure of the pore fluid p_p, pressure of the fracture fluid p_f, temperature of the solid skeleton T_s, temperatures of the pore fluid T_p and of the fracture fluid T_f. These primary unknowns are interpolated within the generic element e, in terms of nodal values through the interpolation functions $\mathbf{N}_\mathbf{u}$, $\mathbf{N}_p$, $\mathbf{N}_T$, respectively,

$$
\mathbf{u} = \mathbf{N}_\mathbf{u}\mathbf{u}^e, \qquad p_p = \mathbf{N}_p\,\mathbf{p}_p^e, \qquad p_f = \mathbf{N}_p\,\mathbf{p}_f^e, \qquad T_k = \mathbf{N}_T\,\mathbf{T}_k^e, \quad k \in \mathcal{K}.
\tag{51}
$$

Multiplying equations (12)-(16) by the virtual fields $\delta\mathbf{u}$, δp, and δT, and integrating by parts over the body V, provides the weak form of the problem,

$$
\int_V \nabla(\delta\mathbf{u}) :\, \boldsymbol{\sigma} - \delta\mathbf{u}\cdot\mathbf{F}\,\mathrm{d}V = \int_{\partial V} \delta\mathbf{u}\cdot\boldsymbol{\sigma}\cdot\hat{\mathbf{n}}\,\mathrm{d}S,
\tag{52}
$$

$$
\int_V \nabla(\delta p)\cdot\mathbf{J}_k - \delta p\, f_k\,\mathrm{d}V = \int_{\partial V} \delta p\,\mathbf{J}_k\cdot\hat{\mathbf{n}}\,\mathrm{d}S, \quad k \in \mathcal{K}^*
\tag{53}
$$

$$
\int_V \nabla(\delta T)\cdot\mathbf{q}_k - \delta T\,\mathcal{L}_k\,\mathrm{d}V = \int_{\partial V} \delta T\mathbf{q}_k\cdot\hat{\mathbf{n}}\,\mathrm{d}S, \quad k \in \mathcal{K},
\tag{54}
$$

where $\hat{\mathbf{n}}$ is the unit outward vector normal to the boundary ∂V. A standard Galerkin procedure is adopted for the whole system of equations (52)-(54). Specific stabilization *ad hoc* for forced convection, such as the Streamline Upwind / Petrov-Galerkin method, is required only if a hard outflow boundary condition is applied on the temperature field. The resulting non-linear first-order semi-discrete equations for the unknown vector $\mathbb{X}$,

$$
\mathbb{X} = [\mathbf{u} \quad \mathbf{p}_p \quad \mathbf{p}_f \quad \mathbf{T}_s \quad \mathbf{T}_p \quad \mathbf{T}_f]^{\mathrm{T}}
\tag{55}
$$

with maximum nodal length = dimension of space + 5, imply the residual $\mathbb{R}$ to vanish:

$$
\mathbb{R} = \mathbb{F}^{\mathrm{surf}}(\mathbb{S}, \mathbb{X}) - \mathbb{F}^{\mathrm{int+conv}}\left(\mathbb{X}, \frac{\mathrm{d}\mathbb{X}}{\mathrm{d}t}\right) = \mathbb{O},
\tag{56}
$$

Here $\mathbb{F}^{\text{int+conv}}$ is the vector that contains the internal forces together with the convective contributions appearing on the left-hand-side of eqn (52)-(54), and $\mathbb{F}^{\text{surf}}$ is the vector of surface loadings denoted collectively $\mathbb{S}$. The semi-discrete equations are integrated through a generalized trapezoidal rule defined by a scalar $\alpha \in]0,1]$. At step $n+1$, the equations are enforced at time $t_{n+\alpha} = t_n + \alpha\,\Delta t$, with $\Delta t = t_{n+1} - t_n$, namely,

$$\mathbb{R}_{n+\alpha} \;=\; \mathbb{F}^{\text{surf}}\left(\mathbb{S}_{n+\alpha}, \mathbb{X}_{n+\alpha}\right) - \mathbb{F}^{\text{int+conv}}\left(\mathbb{X}_{n+\alpha}, \mathbb{V}_{n+\alpha}\right) = \mathbb{O}\,. \tag{57}$$

In the above relation, $\mathbb{Z} = \mathbb{S}, \mathbb{X}, \mathbb{V}$ are defined as $\mathbb{Z}_{n+\alpha} = (1-\alpha)\,\mathbb{Z}_n + \alpha\,\mathbb{Z}_{n+1}$, and $\mathbb{X}_{n+1}$ and $\mathbb{V}_{n+1}$ are approximations of $\mathbb{X}(t_{n+1})$ and $(\mathrm{d}\mathbb{X}/\mathrm{d}t)(t_{n+1})$, respectively. The system (57) is solved iteratively by an explicit-implicit operator split, Hughes [1987], namely at step n, iteration $i+1$,

$$\mathbb{R}^{i+1}_{n+\alpha} \;=\; \mathbb{F}^{\text{surf}}_{\text{E}}\left(\mathbb{S}_{n+\alpha}, \mathbb{X}^{i}_{n+\alpha}\right) - \mathbb{F}^{\text{int+conv}}_{\text{I}}\left(\mathbb{X}^{i+1}_{n+\alpha}, \mathbb{V}^{i+1}_{n+\alpha}\right) = \mathbb{O}. \tag{58}$$

The partition shown in equation (58) is motivated by two observations: (1) the dependence of the vector of external forces on the solution is weak; (2) the vector of internal forces depends non-linearly on the solution $\mathbb{X}$ through the non-linear field equations (43)-(49). The global iteration process uses a full Newton-Raphson procedure. The Newton direction $\Delta\mathbb{V}$ is sought by setting the residual eqn (58) to zero,

$$\mathbb{R}^{i+1}_{n+\alpha} \;=\; \mathbb{R}^{i}_{n+\alpha} - \mathbb{C}\,\left(\alpha\,\Delta\mathbb{V}\right) \;=\; \mathbb{O}\,. \tag{59}$$

$\mathbb{R}^{i}_{n+\alpha}$ represents the *exact* non-linear contributions of the comprehensive model, whereas the *effective diffusion matrix* $\mathbb{C}$ is expressed in terms of the global diffusion matrix $\mathbb{D} = \mathbb{D}(\mathbb{X}, \mathbb{V})$ and of the global stiffness-convection matrix $\mathbb{K} = \mathbb{K}(\mathbb{X}, \mathbb{V})$,

$$\mathbb{C} = \mathbb{D} + \mathbb{K}\,\alpha\,\Delta t. \tag{60}$$

The global diffusion and stiffness-convection matrices are obtained by assembling the element contributions which have the following block structure,

$$\mathbb{D}^e = \begin{bmatrix} 0 & 0 & 0 & 0 & 0 & 0 \\ \mathbf{D}^e_{p_p\,\mathbf{u}} & \mathbf{D}^e_{p_p\,p_p} & \mathbf{D}^e_{p_p\,p_f} & \mathbf{D}^e_{p_p\,T_s} & \mathbf{D}^e_{p_p\,T_p} & 0 \\ \mathbf{D}^e_{p_f\,\mathbf{u}} & \mathbf{D}^e_{p_f\,p_p} & \mathbf{D}^e_{p_f\,p_f} & \mathbf{D}^e_{p_f\,T_s} & 0 & \mathbf{D}^e_{p_f\,T_f} \\ \mathbf{D}^e_{T_s\mathbf{u}} & \mathbf{D}^e_{T_sp_p} & \mathbf{D}^e_{T_sp_f} & \mathbf{D}^e_{T_sT_s} & 0 & 0 \\ 0 & \mathbf{D}^e_{T_pp_p} & 0 & 0 & \mathbf{D}^e_{T_pT_p} & 0 \\ 0 & 0 & \mathbf{D}^e_{T_fp_f} & 0 & 0 & \mathbf{D}^e_{T_fT_f} \end{bmatrix}, \tag{61}$$

$$\mathbb{K}^e = \begin{bmatrix} \mathbf{K}^e_{\mathbf{uu}} & \mathbf{K}^e_{\mathbf{u}p_p} & \mathbf{K}^e_{\mathbf{u}p_f} & \mathbf{K}^e_{\mathbf{u}T_s} & 0 & 0 \\ 0 & \mathbf{K}^e_{p_p\,p_p} & \mathbf{K}^e_{p_p\,p_f} & 0 & \mathbf{K}^e_{p_p\,T_p} & \mathbf{K}^e_{p_p\,T_f} \\ 0 & \mathbf{K}^e_{p_f\,p_p} & \mathbf{K}^e_{p_f\,p_f} & 0 & \mathbf{K}^e_{p_f\,T_p} & \mathbf{K}^e_{p_f\,T_f} \\ 0 & 0 & 0 & \mathbf{K}^e_{T_sT_s} & \mathbf{K}^e_{T_sT_p} & \mathbf{K}^e_{T_sT_f} \\ 0 & \mathbf{K}^e_{T_pp_p} & \mathbf{K}^e_{T_pp_f} & \mathbf{K}^e_{T_pT_s} & \mathbf{K}^e_{T_pT_p} & \mathbf{K}^e_{T_pT_f} \\ 0 & \mathbf{K}^e_{T_fp_p} & \mathbf{K}^e_{T_fp_f} & \mathbf{K}^e_{T_fT_s} & \mathbf{K}^e_{T_fT_p} & \mathbf{K}^e_{T_fT_f} \end{bmatrix}. \tag{62}$$

The detailed expression of these matrices is provided in Appendix B. The finite element code has been developed as part of this work. The four-node element (QUAD4) is used to interpolate all unknowns. The number of integration points is equal to two (in each spatial dimension), for all matrices and all residuals including the convective contributions. Iterations are stopped when the tolerances below involving both the *overall scaled* residual and unknowns are satisfied:

tol_1: $\quad \left|\mathbb{R}^i\right| / \left|\mathbb{R}^1\right| < 0.001$

tol_2: $\quad \left|x^i - x^{i-1}\right| / \left|x^i\right| < 0.001, \quad$ for $x = u_j, p_p, p_f, T_s, T_p, T_f$.

Each component of the residual vector is scaled by a representative value for the problem at hand as detailed in Gelet et al. [2012].

The time integration parameter α is taken equal to 2/3. Conditional stability characterizes non-linear transient convective-diffusive problems discretized with a full Newton-Raphson scheme, Belytschko and Hughes [1983]. The time step Δt is increased by fits and starts in the range $[\Delta t_{\min},\ \Delta t_{\max}]$ in order to keep the computation time within acceptable limits. The average number of Newton-Raphson iterations per time step has been observed to remain around 5. The lower bound $\Delta t_{\min}$ is associated with the fastest diffusion time and is maintained constant until hydraulic steady state is reached, whereas $\Delta t_{\max}$ is associated with the slowest remaining diffusion process.

To increase the accuracy of the solution in the vicinity of the injection well, the mesh is graded along the vertical direction according to a logarithmic rule.

6. HDR reservoir analysis

The thermo-hydro-mechanical constitutive equations are now used to investigate generic HDR reservoirs with various fracture spacings B subjected to temperature gradients.

6.1. Geometry of the HDR reservoir

An artificially fractured reservoir with horizontal injection and production wells is considered (Figure 1). The injection and the production wells are located at the bottom and at the top of the reservoir, respectively, and they penetrate the entire horizontal extent of the problem domain x_R. The problem definition requires information on the horizontal and vertical extents of the reservoir x_R and z_R respectively, on the average fracture spacing B, on the average fracture aperture $2\,b$ and on the average permeability of the porous blocks k_p, also referred to as the second porosity. The simulations assume a plane strain analysis, and the finite element mesh includes only half of the reservoir.

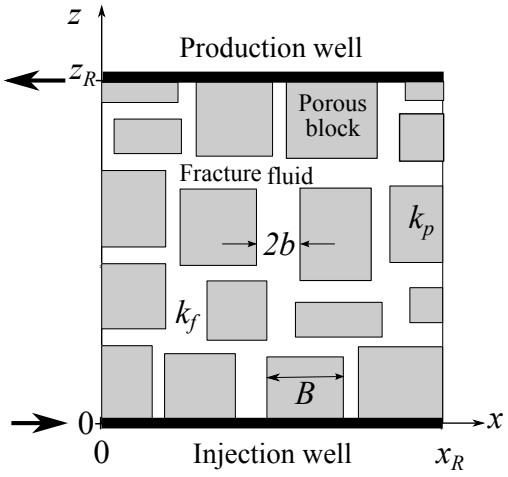

Figure 1: Representation of a generic HDR reservoir. The exact convective flow path is unknown and only the average fracture spacing B and n_f the porosity of the fracture network are required to obtain the average fracture aperture $2\,b$, eqn (65). k_p and k_f denote the permeabilities of the porous blocks and of the fracture network, respectively. The simulations assume a plane strain analysis, in the $x-z$ plane. Symmetry with respect to z-axis is assumed.

6.2. Initial and boundary conditions

Prior to the circulation test, the reservoir is assumed to be in local thermal equilibrium, and the solid and the fluids have identical temperatures $T^0 = T_s^0 = T_p^0 = T_f^0$. Geothermal gradient is neglected. The initial pressures of the fluids $p_p^0 = p_f^0 = \rho_f g z_{\rm av}$ are assumed to be in hydrostatic equilibrium, proportional to the depth $z_{\rm av}$, with the fluid densities $\rho_p = \rho_f$. The initial stress state is due to the overburden stress $\sigma_z^0 = \sigma_{\rm v}$ and to the lateral earth stress $\sigma_x^0 = \sigma_H$. Since, the fluids are initially in local thermal and hydraulic equilibria, the reference thermodynamic potentials of the fluids are equal: $S^0 = S_p^0 = S_f^0$, $G^0 = G_p^0 = G_f^0$, and $H^0 = H_p^0 = H_f^0$.

The thermal, hydraulic and mechanical boundary conditions (BC) are shown in Figure 2.

(1) Thermal boundary conditions:

The injection temperature is applied to all the phases along the injection well ($x \in [0, x_R]$, $z = 0$). The remaining boundaries ($x = 0$, $z \in]0, z_R]$), ($x \in [0, x_R]$, $z = z_R$) and ($x = x_R$, $z \in]0, z_R]$) are insulated from the surroundings, that is $\mathbf{q}_s \cdot \hat{\mathbf{n}} = \mathbf{q}_p \cdot \hat{\mathbf{n}} = \mathbf{q}_f \cdot \hat{\mathbf{n}} = 0$, $\hat{\mathbf{n}}$ being the unit outward normal to the reservoir.

(2) Hydraulic boundary conditions:

The injection and production pressures, denoted p_{inj} and p_{out}, are specified along the injection and the production wells, respectively, for the two fluid phases so that $p_p(x \in [0, x_R],\, z = 0) = p_f(x \in [0, x_R],\, z = 0) = p_{\text{inj}}$ and $p_p(x \in [0, x_R],\, z = z_R) = p_f(x \in [0, x_R],\, z = z_R) = p_{\text{out}}$. The remaining boundaries ($x = 0$, $z \in]0, z_R[$) and ($x = x_R$, $z \in]0, z_R[$) are impermeable, i.e. $\mathbf{J}_p \cdot \hat{\mathbf{n}} = \mathbf{J}_f \cdot \hat{\mathbf{n}} = 0$.

(3) Mechanical boundary conditions:

The vertical stress $\sigma_z = \sigma_z^0$ remains constant along the top boundary ($x \in [0, x_R]$, $z = z_R$) and similarly for the horizontal stress $\sigma_x = \sigma_x^0$ along the lateral boundary ($x = x_R$, $z \in [0, z_R]$), while the displacements on the other boundaries are specified as $u_x(x = 0,\, z \in [0, z_R]) = 0$ and $u_z(x \in [0, x_R],\, z = 0) = 0$.

The influences of the spatial uniformity of the flow path and of the external heat supply on the thermal depletion of the reservoir have been addressed in Gelet [2011]. They are disregarded herein so as to focus on the specific influence of the dual porosity model.

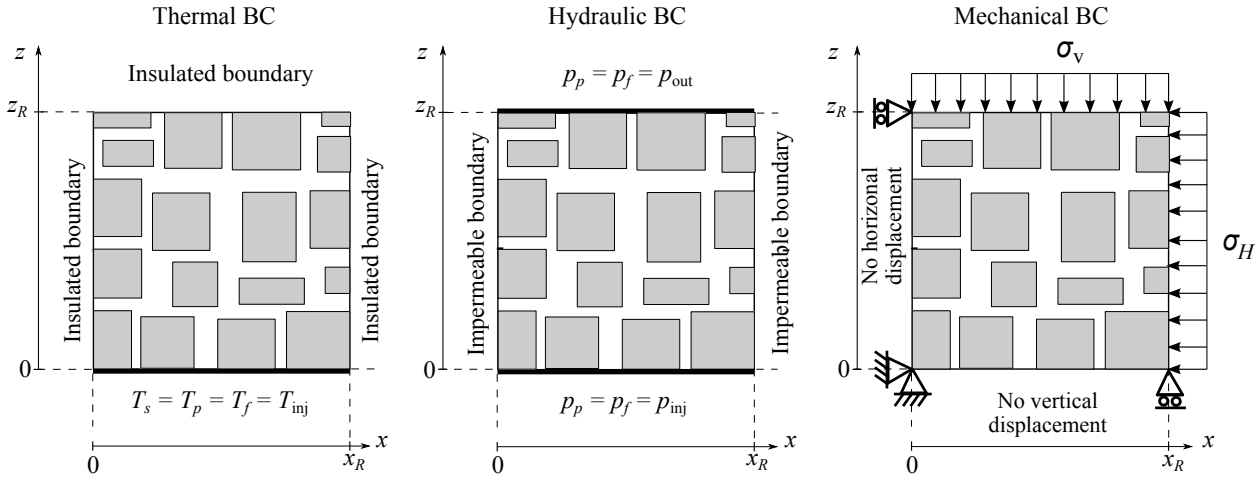

Figure 2: Thermal, hydraulic and mechanical boundary conditions (BC). Symmetry with respect to z-axis is assumed.

6.3. Parameters related to the fracture spacing B

The fracture spacing B influences three material parameters used in the model, namely (1) the leakage parameter η [1/Pa.s], (2) the specific solid-to-fracture fluid heat transfer coefficient κ_{sf} [W/m^3.K] and (3) the specific pore fluid-to-fracture fluid heat transfer coefficient κ_{pf} [W/m^3.K].

(1) The leakage parameter $\eta = \bar{\alpha}\, k_p/\mu_p \geq 0$ that controls the flow between the porous blocks and the fracture network draws from Barenblatt et al. [1960]. In this double porosity context, the leakage parameter does not treat the two cavities symmetrically, and puts emphasis on the permeability of the porous blocks k_p which is lower than the permeability of the fracture network. The aperture factor $\bar{\alpha}$ [1/m^2] corresponding to the lowest permeable phase has been introduced by Warren and Root [1963],

$$\eta = \bar{\alpha}\, \frac{k_p}{\mu_p}, \quad \text{with} \quad \bar{\alpha} = \frac{4n(n+2)}{B^2}\,, \tag{63}$$

in which n represents the space dimension.

(2) The specific solid-to-fracture fluid heat transfer coefficient κ_{sf} is usually defined as the product of the solid-to-fracture fluid specific surface S^s_{sf} [m^2/m^3] with the coefficient of solid-to-fracture fluid heat transfer h_{sf} [W/m^2.K],

$$\kappa_{sf} = h_{sf} \times S^s_{sf}, \quad \text{with} \quad S^s_{sf} = \frac{4n^s}{B} \quad \text{for} \quad 2\,b \ll B\,. \tag{64}$$

where the specific surface S^s_{sf} is obtained by considering a porous block square of size B bordered by a fracture fluid of width b. The specific surface S^s_{sf} represents the ratio of the wetted solid surfaces over the total volume, de Marsily [1981]. The volume fraction n^f of the fracture fluid is then equal to

$$n^f = \frac{2 \times 2\,b}{B} \quad \text{for} \quad 2\,b \ll B\,, \tag{65}$$

so that, for a given fracture porosity n^f, the average fracture aperture $2b$ increases with the fracture spacing B. By assuming that the effect of convection in the fracture fluid phase (perpendicular to the solid-fracture fluid interface) is negligible, the coefficient of solid-to-fracture fluid heat transfer h_{sf} may be quantitatively characterized by the sum of the thermal resistances of the two phases in series, Bejan [1993],

$$\frac{1}{h_{sf}} = \frac{2\,b}{2n^f \Lambda_f} + \frac{B}{2n^s \Lambda_s}\,, \tag{66}$$

By inserting eqs (65) and (66) in eqn (64), the specific coefficient of heat transfer between the solid and the fracture fluid κ_{sf} is, in turn, linearly related to B^{-2},

$$\kappa_{sf} = \frac{8\,n^s}{B^2}\,\frac{n^s\Lambda_s \times 2\,\Lambda_f}{n^s\Lambda_s + 2\Lambda_f}\,. \tag{67}$$

It is worth noting that if $n^s\Lambda_s \ll 2\Lambda_f$, the above relation reduces to $\kappa_{sf} = 8\,(n^s)^2\Lambda_s/B^2$ where the formulation does not treat the two phases symmetrically, *à la* Warren and Root [1963], and puts emphasis on the most insulating phase.

(3) Similarly, the specific pore fluid-to-fracture fluid heat transfer coefficient κ_{pf} is defined as the product of the pore fluid-to-fracture fluid specific surface S^s_{pf} [m^2/m^3] with the coefficient of pore fluid-to-fracture fluid heat transfer h_{pf} [W/m^2.K],

$$\kappa_{pf} = h_{pf} \times S^s_{pf} = \frac{8\,(n^p)^2\Lambda_p}{B^2}, \quad \text{with} \quad S^s_{pf} = \frac{n^p}{n^s} \times S^s_{sf} \quad \text{and} \quad h_{pf} \approx \frac{2n^p\Lambda_p}{B}\,, \tag{68}$$

for $\Lambda_p = \Lambda_f$, $2b \ll B$ and $n^p \ll 1$.

Consequently, the three coefficients η, κ_{sf} and κ_{pf} scale with the inverse of the square of the fracture spacing B^{-2}, as illustrated in Table 1.

Parameter	Unit	Eqn	Fracture spacing B [m]				
			0.01	1	10	13	20
η	[1/Pa.s]	(63)	$3.2\,10^{-12}$	$3.2\,10^{-16}$	$3.2\,10^{-18}$	$1.88\,10^{-18}$	$8.0\,10^{-19}$
κ_{sf}	[W/m^3.K]	(67)	$6.18\,10^{4}$	6.18	$6.18\,10^{-2}$	$3.50\,10^{-2}$	$1.54\,10^{-2}$
κ_{pf}	[W/m^3.K]	(68)	$1.2\,10^{2}$	$1.2\,10^{-2}$	$1.2\,10^{-4}$	$7.07\,10^{-5}$	$3.0\,10^{-5}$

Table 1: Sensitivity of the leakage parameter η, the specific solid-to-fracture fluid heat transfer coefficient κ_{sf} and the specific pore fluid-to-fracture fluid heat transfer coefficient κ_{pf} to the fracture spacing B for a two-dimensional fracture network $n = 2$ endowed with a pore permeability $k_p = 10^{-20}$ m^2, a fracture porosity $n^f = 0.005$ and a pore porosity $n^p = 0.05$. The other material parameters are taken from Table 4.

Correlations of the solid-to-fracture fluid heat transfer coefficient h_{sf} have been proposed in the literature, with the Nusselt number, Wakao and Kaguei [1982], and with a capillary tube model, Zanotti and Carbonell [1984]. Few experimental works have investigated the magnitude of this coefficient, Pecker and Deresiewicz [1973], Jiang et al. [2006]. Instead, here, a calibration of the model with help of data provided from the two HDR reservoirs of Fenton Hill and Rosemanowes is proposed (Section 7). A sensitivity analysis is performed in Subsection 8.2 to determine the influence of the fracture spacing B on the results.

Boundary conditions	Value	Unit	Reference
Injection temperature T_{inj}	70	°C	Fig. 6-1, Zyvoloski et al. [1981]
Initial in-situ temperature $T_s^0 = T_p^0 = T_f^0$	178	°C	Fig. 6-3, Zyvoloski et al. [1981]
Production pressure $p_{\text{out}} = \rho_f g z$ at $z = 2.673\,\text{km}$	26.19	MPa	-
Injection pressure $p_{\text{inj}} = \rho_f g z$ at $z = 2.903\,\text{km}$	28.44	MPa	-
Overburden compressive stress σ_{v}	-75.0	MPa	Murphy et al. [1977]
Earth compressive stress σ_H	-37.5	MPa	Murphy et al. [1977]

Table 2: Initial and loading boundary conditions representative of Fenton Hill HDR reservoir, run segment 5.

Boundary conditions	Value	Unit	Reference
Injection temperature T_{inj}	23	°C	Hicks et al. [1996]
Initial in-situ temperature $T_s^0 = T_p^0 = T_f^0$	83.5	°C	Richards et al. [1994]
Production pressure $p_{\text{out}} = \rho_f g z$ at $z = 2.160\,\text{km}$	21.12	MPa	-
Injection pressure $p_{\text{inj}} = \rho_f g z$ at $z = 2.490\,\text{km}$	24.35	MPa	-
Overburden compressive stress σ_{v} at $z_{\text{av}} = 2.325\,\text{km}$	-60.4	MPa	Bruel [1995]
Earth compressive stress σ_H at $z_{\text{av}} = 2.325\,\text{km}$	-65.11	MPa	Bruel [1995]

Table 3: Initial and loading boundary conditions representative of Rosemanowes HDR reservoir, RH12/RH15 system.

Material parameter	Value	Unit	Reference
Drained Young's modulus E	38.9	GPa	Murphy et al. [1977]
Drained Poisson's ratio ν	0.3	-	Murphy et al. [1977]
Volumetric thermal expansion c_T	3.3×10^{-6}	1/K	Zyvoloski et al. [1981]
Compressibility ratio c_p/c^{DS}	0.9	-	Wilson and Aifantis [1982]
Fracture network porosity n^f	< 0.01	-	Murphy et al. [1977]
Porosity of the porous blocks n^p	$10 \times n^f$	-	1
Fracture network permeability k_f	$< 10^{-13}$	m^2	Murphy et al. [1977]
Permeability of the porous blocks k_p	$\geq 10^{-20}$	m^2	Murphy et al. [1977]
	$\leq 10^{-18}$	m^2	Murphy et al. [1977]
Solid grains compressibility c_s	2.7×10^{-11}	1/Pa	Murphy et al. [1977]
Solid thermal diffusivity $\alpha_{T,s}$	1.1×10^{-6}	m^2/s	Elsworth [1989]
Solid thermal conductivity Λ_s	2.71	W/m.K	Elsworth [1989]
Solid specific heat capacity $C_s^{(v)}$	948.55	J/kg.K	2
Solid density ρ_s	2600	kg/m^3	2
Fluid compressibilities $c_{pH} = c_{fH}$	4.54×10^{-10}	1/Pa	2
Fluid thermal expansion $c_{pT} = c_{fT}$	10^{-3}	1/K	2
Fluid dynamic viscosities $\mu_p = \mu_f$	3×10^{-4}	Pa.s	2
Fluid thermal conductivities $\Lambda_p = \Lambda_f$	0.6	W/m.K	2
Thermo-osmosis coefficients $\Theta_p = \Theta_f$	0	$\text{m}^2/\text{s.K}$	2
Fluid specific heat capacities $C_p^{(p)} = C_f^{(p)}$	4275	J/kg.K	Elsworth [1989]
Fluid densities $\rho_p = \rho_f$	980.0	kg/m^3	2
Fluid thermal diffusivities $\alpha_{T,p} = \alpha_{T,f}$	1.58×10^{-7}	m^2/s	-
Solid-to-pore fluid heat transfer coef. κ_{sp}	10^4	$\text{W/m}^3\text{.K}$	3

Table 4: Input parameters representative of Fenton Hill HDR reservoir, run segment 5. 1. First estimation owing to the rather high pressure of the overburden rock. 2: Estimated parameters for water. 3. Local thermal equilibrium is enforced between the pore fluid phase and the solid phase owing to the absence of convection, to their similar thermal diffusivities $\alpha_{T,s} \approx \alpha_{T,p} \times 10$, and to the large specific surface S_{sp}^s.

Unless the fracture spacing tends to zero, the dual porosity model will *not* recover the response of the single porosity model since it accounts for the presence of the pore fluid in the balance of momentum and in

Material parameter	Value	Unit	Reference
Drained Young's modulus E	40.0	GPa	Bruel [1995]
Drained Poisson's ratio ν	0.25	-	Armstead and Tester [1987]
Volumetric thermal expansion c_T	3.3×10^{-6}	1/K	1
Compressibility ratio c_p/c^{DS}	0.9	-	Wilson and Aifantis [1982]
Fracture network porosity n^f	< 0.01	-	Richards et al. [1994]
Porosity of the porous block n^p	$10 \times n^f$	-	2
Fracture network permeability k_f	$\leq 10^{-13}$	m^2	Bruel [1995]
Permeability of the porous block k_p	10^{-18}	m^2	Richards et al. [1994]
Solid grains compressibility c_s	2.0×10^{-11}	1/Pa	1
Solid thermal diffusivity $\alpha_{T,s}$	1.29×10^{-6}	m^2/s	-
Solid thermal conductivity Λ_s	2.8	W/m.K	Bruel [1995]
Solid specific heat capacity $C_s^{(v)}$	822.1	J/kg.K	Kolditz and Clauser [1998]
Solid density ρ_s	2642	kg/m^3	Kolditz and Clauser [1998]
Fluid hydraulic compressibilities $c_{pH} = c_{fH}$	4.54×10^{-10}	1/Pa	1
Fluid thermal compressibilities $c_{pT} = c_{fT}$	0.65×10^{-3}	1/K	1
Fluid dynamic viscosities $\mu_p = \mu_f$	6×10^{-4}	Pa.s	Richards et al. [1994]
Fluid thermal conductivities $\Lambda_p = \Lambda_f$	0.68	W/m.K	Kolditz and Clauser [1998]
Thermo-osmosis coefficients $\Theta_p = \Theta_f$	0	m^2/s.K	1
Fluid specific heat capacities $C_p^{(p)} = C_f^{(p)}$	4219.8	J/kg.K	Kolditz and Clauser [1998]
Fluid densities $\rho_p = \rho_f$	978.0	kg/m^3	Kolditz and Clauser [1998]
Fluid thermal diffusivities $\alpha_{T,p} = \alpha_{T,f}$	1.67×10^{-7}	m^2/s	-
Solid-to-pore fluid heat transfer coefficient κ_{sp}	10^4	W/m^3.K	3

Table 5: Input parameters representative of Rosemanowes HDR reservoir. 1: Estimated parameters for water or granite. 2. First estimation owing to the rather high pressure of the overburden rock. 3. Local thermal equilibrium is enforced between the pore fluid phase and the solid phase owing to the absence of convection, to their similar thermal diffusivities $\alpha_{T,s} \approx \alpha_{T,p} \times 10$, and to the large specific surface S_{sp}^s.

the balance of energy equations, while the single porosity model does not recognize the pore fluid.

7. Calibration with field data

The thermal response obtained from the thermo-hydro-mechanical model may be compared with field results from the literature. Two hot dry rock reservoirs are investigated: (1) Fenton Hill, New Mexico, USA, and (2) Rosemanowes, Cornwall, UK. The time profiles of the fracture fluid temperature (at the production well) are scrutinized alone in Figure 3, although the numerical results presented in this section describe a complete thermo-hydro-mechanical problem. The response in terms of fluid pressures and effective stress will be studied in Section 8 for Fenton Hill HDR reservoir only. The reservoirs are described with a dual porosity model in LTNE and the simulations assume a plane strain analysis. Furthermore, the triple point of water is used as a reference, Kestin [1966], p. 513, so that the reference entropy and chemical potential are set to $S^0 = 2.101\,\text{kJ/K.kg}$ and $G^0 = -187.6\,\text{kJ/kg}$, respectively.

For a LTNE analysis, the time profile of the temperature depletion is characterized by three stages: (a) the first stage represents the abrupt propagation of the injection temperature dominated by convection; (b) the second stage characterizes the heat transfer between the fracture fluid phase and the porous blocks and (c) the third stage represents the final thermal depletion of the porous medium. The least well-defined of the material parameters required for a thermo-hydro-mechanical simulation in LTNE are the fracture permeability k_f, the fracture porosity n^f and the solid-to-fracture fluid *specific* heat transfer coefficient κ_{sf}. These coefficients are calibrated so that the numerical response matches the field response based on the following procedure: (i) the fracture network permeability k_f is obtained so that the end of the first stage matches the field data; (ii) the fracture network porosity n^f is adjusted so that the duration of the second

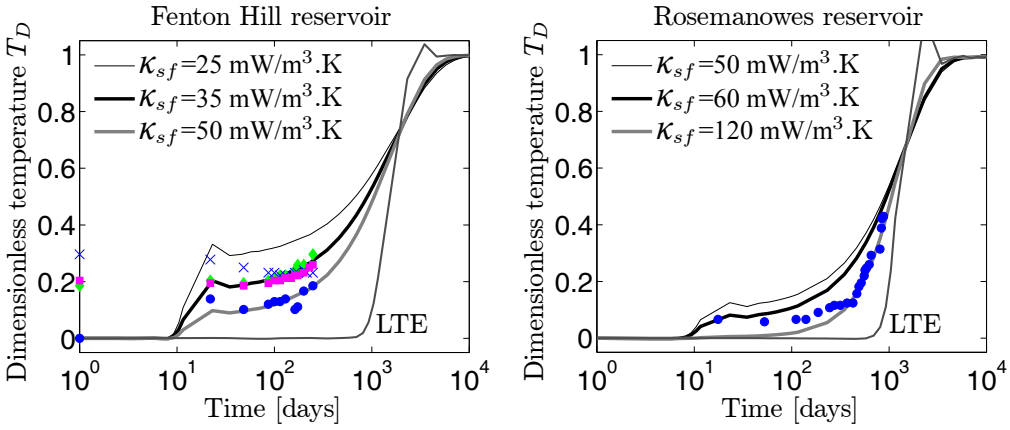

Figure 3: Relative temperature outlet $T_D = (T^0 - T_f(z = z_R))/(T^0 - T_{\text{inj}})$ versus time in days. LTE stands for local thermal equilibrium and is obtained for $\kappa_{sf} = 100\,\text{W/m}^3\text{.K}$. *Colors are available on the electronic version.* (left) Fenton Hill hot dry rock reservoir with $k_f = 10^{-14}\,\text{m}^2$ and $n^f = 0.005$. Field data pertain to ∘ 2703 m, ⋄ 2673 m, × 2626 m and □ in the casing 2660 m, Zyvoloski et al. [1981]. The optimum specific solid-to-fracture fluid heat transfer coefficient κ_{sf} is equal to $35\,\text{mW/m}^3\text{.K}$. (right) Rosemanowes hot dry rock reservoir with $k_f = 10^{-13}\,\text{m}^2$, $n^f = 0.005$. Field data pertain to ∘ the casing shoe of the production well (≈ 2125 m in true vertical depth), Kolditz and Clauser [1998]. The optimum specific solid-to-fracture fluid heat transfer coefficient κ_{sf} lies in the range 60 to $120\,\text{mW/m}^3\text{.K}$. The late overshooting oscillations for the LTE solution are due to an imperfect damping of the convective contribution, Gelet et al. [2012].

stage matches the rest of the response and (iii) the optimum solid-to-fracture fluid heat transfer coefficient κ_{sf} is obtained so that the magnitude of the second stage best fits the field data.

7.1. Fenton Hill reservoir

The circulation test was induced between the depths 2903 m and 2667 m with an average reservoir height of $z_R = 230\,\text{m}$. Experimental results for the test 'segment-5' are reported in Zyvoloski et al. [1981]. The horizontal half-width of the permeable reservoir is arbitrarily chosen equal to $x_R = 200\,\text{m}$. Appropriate loading boundary conditions and material parameters are documented in Tables 2 and 4, in which the hydrostatic pressure gradient between the injection and the production wells is imposed.

The thermo-hydro-mechanical model for this LTNE analysis recovers well the field response for the combination of fracture permeability $k_f = 10^{-14}\,\text{m}^2$, fracture porosity $n^f = 0.005$ and *specific* solid-to-fracture fluid heat transfer coefficient $\kappa_{sf} = 35\,\text{mW/m}^3\text{.K}$. This set of calibrated parameters is the same as for a single porosity model if the thermal diffusivity of the solid phase is replaced by the thermal diffusivity of the porous blocks (the 'equivalent' solid phase).

If the calibrated material parameters are considered suitable, the fracture spacing can be calculated with eqn (67), $B = 13\,\text{m}$ which matches well the 10 m magnitude proposed in Figure 3.2 of Zyvoloski et al. [1981]. Furthermore, the solid-to-fracture fluid heat transfer coefficient h_{sf} can be estimated to $h_{sf} = 0.12\,\text{W/m}^2\text{.K}$.

It is worth noting that the field data for Fenton Hill reservoir display spatially heterogeneous initial rock temperatures, Zyvoloski et al. [1981]. This situation is attributed to circulation in the hot dry rock reservoir before the circulation tests. The initial temperature T^0 used to calculate the relative temperature T_D and to perform the calibrations in Figure 3, left, represents the temperature at the lowest outlet point $z = 2703\,\text{m}$. If the initial temperature T^0 is chosen at a higher outlet point $z > 2703\,\text{m}$, the calibrations hold for higher values of the solid-to-fracture fluid heat transfer κ_{sf}.

7.2. Rosemanowes reservoir

This second circulation test was performed between the depths 2490 m and 2160 m with an average reservoir height of $z_R = 330\,\text{m}$. The horizontal half-width of the permeable reservoir is arbitrarily chosen equal to $x_R = 200\,\text{m}$. Appropriate loading boundary conditions and material parameters are documented in Tables 3 and 5. The setup and the boundary conditions are similar to the Fenton Hill simulation so as to simplify the implementation. The experimental results for the RH12/RH15 system reported in Kolditz and Clauser [1998], their Figure 5, provide the data for the calibration.

The thermo-hydro-mechanical LTNE model recovers well the field response for the combination of fracture permeability $k_f = 10^{-13}\,\mathrm{m}^2$, fracture porosity $n^f = 0.005$ and *specific* solid-to-fracture fluid heat transfer coefficient κ_{sf} in the range 60 to 120 $\mathrm{mW/m^3.K}$. The lack of accuracy of the calibration is most probably due to the simplified setup assumed for the numerical simulations: in the field, the wells are not horizontal and the fracture permeability is not uniform within the reservoir. Furthermore, significant water loss (45%) was generated owing to the unconfined nature of the reservoir, Brown et al. [1999], and to its lack of stability, Bruel [2002], leading to the development of short-circuit flow paths.

The calibration of the specific solid-to-fracture fluid heat transfer coefficient κ_{sf} yields the same order of magnitude for both hot dry rock reservoirs, which indicates that the order of magnitude is reliable. The comparisons between the field results and the model simulations demonstrate responses in local thermal non-equilibrium, characterized by three stages, which provides confidence in the LTNE model.

8. Thermo-hydro-mechanical response

The calibration of the thermo-hydro-mechanical model is now used to perform coupled simulations on the Fenton Hill HDR reservoir. Emphasis is laid on delineating the differences in the response of the geothermal system in terms of temperatures, fluid pressures and effective stress, as inferred by the single and dual porosity models. Special attention is devoted to the fracture spacing B. Some details of the constitutive model are also addressed, including the influence of the thermodynamic potentials S^0 and G^0 and the unconnected porosity limit.

For the material parameters associated with Fenton Hill reservoir, we hypothesize that the dual porosity concept will provide a response in the range of a single porosity model and of a dual porosity model endowed with a low pore permeability (lower than the expected value presented in Table 4). Furthermore, the dual porosity model is endowed with a mass transfer law which allows the permeation of fluid from the fractures towards the pores. It is expected that large fracture spacings reduce the thermally induced tensile stress and fluid loss: this phenomenon highlights a key feature of sparsely fractured reservoirs with respect to densely fractured reservoirs.

For the circulation tests simulated, the energy exchanges due to mass transfer $\hat{\rho}_p H_p$ and $\hat{\rho}_f H_f$ appearing in the energy equations of the fluids (48) and (49) have been checked to have virtually no influence on the overall response.

Results are presented in Figures 4 to 12. The sign convention of continuum mechanics is used, compressive stresses being negative.

8.1. Dual porosity model versus single porosity model

The thermo-hydro-mechanical response of fractured media in a LTNE analysis can be sought with two types of models: (2P) models developed for dual porous media involving two pressures and three temperatures or (1P) models developed for single porous media as summarized in Appendix A and involving one pressure and two temperatures. Both types are used to predict the thermo-hydro-mechanical behavior of the Fenton Hill HDR reservoir in Figures 4 and 5. As a simplification here, the (2P) model assumes the temperatures of the solid and of the pore fluid to be identical. Still, two sub-options are considered: (i) the pores are connected to each other with a large permeability $k_p = 10^{-18}\,\mathrm{m}^2$ and (ii) the pores are connected to each other with a low permeability $k_p = 10^{-21}\,\mathrm{m}^2$ so that both the diffusive flow in the pores and the mass transfer are small.

The dual porosity response with a large pore permeability (and hence large mass transfer) is expected to range between the response of the single porosity model (1P), since no pore pressure counterbalance effect is accounted for in the effective stress, and the dual porosity response with a low pore permeability, since the induced pore pressure will dissipate slowly due to the small mass transfer.

The material parameters matching field data for the Fenton Hill HDR reservoir are used, that is, permeability of the fracture network $k_f = 10^{-14}\,\mathrm{m}^2$, volume fraction of the fracture fluid $n^f = 0.005$ and specific solid-to-fracture fluid heat transfer coefficient $\kappa_{sf} = 35\,\mathrm{mW/m^3.K}$. The triple point of water is used as a reference. The initial and loading boundary conditions are detailed in Sect. 6.2. The leakage parameter η is estimated from (63) for the material parameters presented in Table 4 and for the average fracture spacing $B = 13\,\mathrm{m}$ (Sect. 7.1). The vertical profiles at time $t = 3.17$ years of the temperatures, fluid pressures and stress changes from the initial state $\Delta\bar{\boldsymbol{\sigma}} = \bar{\boldsymbol{\sigma}} - \bar{\boldsymbol{\sigma}}^0$ plotted in Figures 4 and 5 illustrate the late time of the

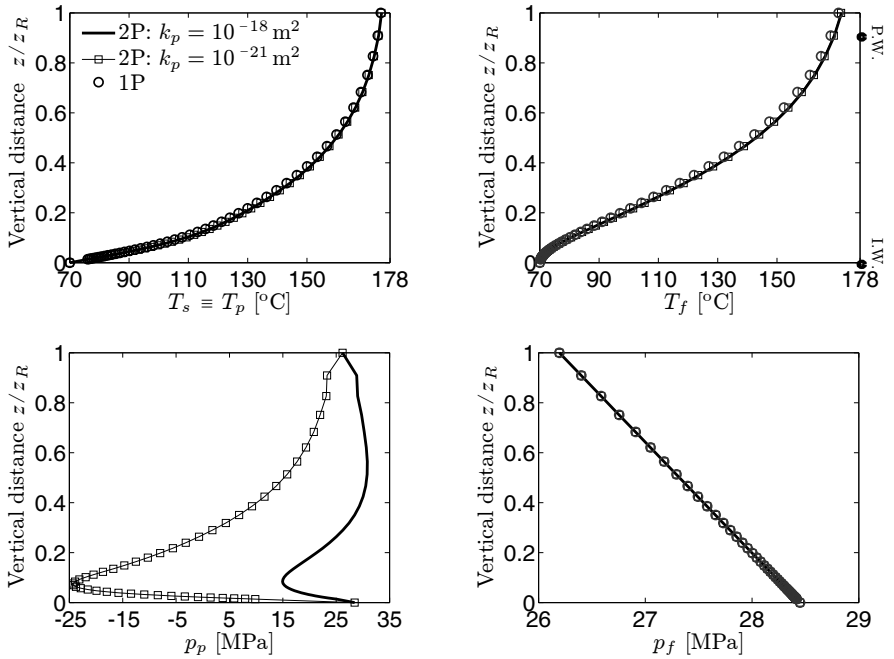

Figure 4: Fenton Hill reservoir, late time ($t = 3.17$ years) vertical profiles of the temperatures of solid and pore fluid (top-left), the temperature of fracture fluid (top-right), the pressure of pore fluid (bottom-left), and the pressure of fracture fluid (bottom-right) for $k_f = 10^{-14}\,\mathrm{m}^2$, $n^f = 0.005$, $\kappa_{sf} = 35\,\mathrm{mW/m^3.K}$ and $B = 13\,\mathrm{m}$ (Sect. 7.1). I.W. stands for injection well and P.W. for production well. The responses of the various models match for the temperatures and for the fracture fluid pressure. On the other hand, the pore pressure response of the dual porosity model displays a pressure drop near the injection point. The magnitude of the pressure drop is controlled by the diffusivity ratio R_p and is larger for smaller pore permeability ($k_p = 10^{-21}\,\mathrm{m}^2$). The single porosity model leaves out of account the pore pressure response. Regarding the pore pressure, the dual porosity response for $k_p = 10^{-18}\,\mathrm{m}^2$ is bounded by the dual porosity response for smaller pore permeabilities and by the fracture fluid pressure (1P), close to the injection well $z/z_R < 0.3$.

numerical test. The coupled thermo-hydro-mechanical response at early time $t = 34.72$ days is presented next in Figure 6.

The coupled behavior of fractured media in thermal and hydraulic non-equilibria is governed by the difference in characteristic times between the thermal depletion of the fracture fluid phase and of the solid/pore fluid phases (Figure 4, top). The significant difference in temperature between the fracture fluid and the porous blocks correlates with their highly distinct masses and volumes. Indeed, heat diffuses by conduction in the porous blocks which are endowed with a large volume $n^s + n^p = 0.995$. On the other hand, the temperature of the fracture fluid propagates by convection and thermal depletion is much faster than in the porous blocks.

The solid temperature responses provided by the single porosity model (1P), the dual porosity model (2P) with a large pore permeability ($k_p = 10^{-18}\,\mathrm{m}^2$) and with a small pore permeability ($k_p = 10^{-21}\,\mathrm{m}^2$) almost match and are not influenced by the pressure and the strain fields. Hence, the calibration proposed in Sect. 7 remains valid for all models.

As expected from the large fracture permeability $k_f = 10^{-14}\,\mathrm{m}^2$, the response of the fracture fluid pressure varies little from one model to the other as opposed to that of the pore fluid pressure. The single porosity model disregards the pore fluid pressure. The dual porosity model displays a decrease in pore pressure induced by the thermal contraction of the solid phase. Indeed, since (1) the pore fluid is embedded into the solid phase which controls fully the magnitude of the thermal contraction and (2) the coefficient of thermal expansion of the fluid c_{pT} is approximatively 300 times greater than that of the solid phase c_T, the pore pressure decrease is governed by the thermal depletion of the solid phase.

On the other hand, the magnitude of the pore pressure peak is controlled by the hydraulic to thermal diffusivity ratio $R_p = \sqrt{\alpha_{H,p}/\alpha_{T,p}}$. The lower R_p, the greater the pore fluid pressure response. Hence, for the dual porosity model with $k_p = 10^{-21}\,\mathrm{m}^2$, R_p is small and the pore pressure drop is large compared with the dual porosity model with $k_p = 10^{-18}\,\mathrm{m}^2$ in which the pore pressure drop dissipates through the

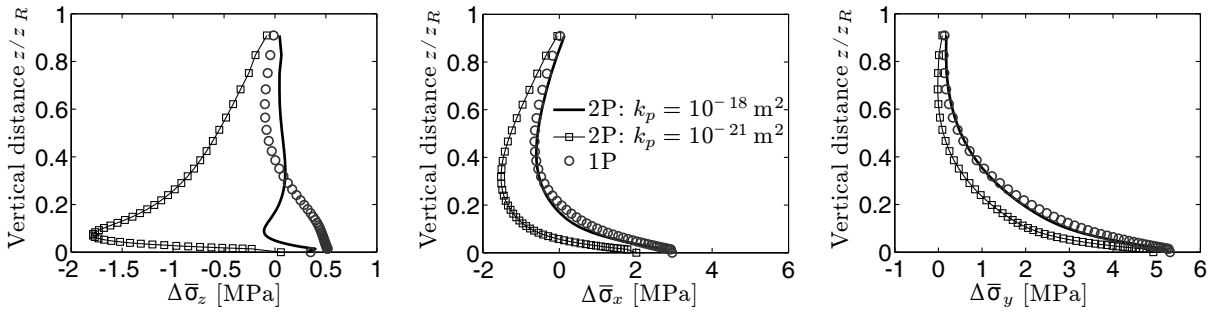

Figure 5: Fenton Hill reservoir, late time ($t = 3.17$ years) vertical profiles of the changes in vertical effective stress (left), lateral effective stress (middle) and out-of-plane effective stress (right). Tensile stresses are counted positive. Owing to the pore pressure contribution, the stress responses described by the single porosity model (1P) are not equivalent to the responses described by the dual porosity model. The single porosity model predicts a thermally induced tensile stress in the vicinity of the injection well, whereas the dual porosity model predicts a smaller tensile stress ($\Delta\bar{\sigma}_x$ and $\Delta\bar{\sigma}_y$) and an increase of compressive stress ($\Delta\bar{\sigma}_z$). The pore pressure drop counterbalances the contraction induced by the solid temperature. As expected, the dual porosity response with $k_p = 10^{-18}$ m^2 is bounded by the single porosity and by the dual porosity with $k_p = 10^{-21}$ m^2 responses, close to the injection well $z/z_R < 0.3$.

connected pores and through mass transfer with the fracture network.

While the thermal depletion of the various phases is the same for all the proposed models, the vertical effective stress is significantly influenced by the pore pressure contribution which tends to damp ($k_p = 10^{-18}$ m^2) or to suppress ($k_p = 10^{-21}$ m^2) the thermally induced tensile stress (1P) (Figure 5). Interestingly, the effective stress response predicted by the dual porosity model for a large pore permeability is bounded by the single porosity response and by the dual porosity response for a small pore permeability, close to the injection well $z/z_R < 0.3$.

The response of the dual porosity model is fully recovered by the single porosity model in the particular case of small fracture spacings $B \to 0$ as presented in the next subsection in Figure 7. This phenomenon is consistent with the fact that, for very small fracture spacings B, fractured media lose their spatial and time scale separation characteristics, which are the two main hypotheses of the dual porosity concept. Once local thermal and hydraulic equilibria are reached, the dual porosity model is indeed expected to reduce to a single porosity model in LTE with porosity equal to the sum of the fracture and pore porosities and permeability equal to the sum of the fracture and pore permeabilities.

Moreover, the early mechanism of fluid loss is a consequence of the law of mass transfer induced by the jump in scaled chemical potentials between the two fluids. During the early time $t = 34.72$ days, the thermal front propagates in the fracture fluid only, while the porous blocks is almost thermally undisturbed as shown in Figure 6 for $k_p = 10^{-21}$ m^2. Consequently, the thermally induced contraction of the pore fluid is small and restricted to the vicinity of the injection well. On the other hand, the temperature difference between the pore fluid and the fracture fluid leads to a large mass transfer from the fractures towards the porous blocks. This large mass transfer is characterized by a large pore pressure drop, to which the thermal contraction contributes a little, and by an increase in compressive effective stress. This model response matches with typical field observations: Murphy et al. [1981] report that the permeation of fluid to the porous blocks is large during the early time and decreases with time.

In summary, the dual porosity model allows a more accurate description of the coupled thermo-hydro-mechanical behavior of fractured reservoirs compared with a single porosity model. In particular, the distinct responses between early time and late time provide information on the permeation mechanism and on the stress path history, which is a key element in view of damage prediction.

8.2. Influence of the fracture spacing B

In Subsection 6.3, the leakage parameter $\eta \propto B^{-2}$, the specific solid-to-fracture fluid heat transfer coefficient $\kappa_{sf} \propto B^{-2}$ and the specific pore fluid-to-fracture fluid heat transfer coefficient $\kappa_{pf} \propto B^{-2}$ have been estimated based on the fracture spacing B. The latter controls *simultaneously* the mass transfer and the heat transfer. The influence of the fracture spacing B is considered in the range from 0 to 20 m, so that the lower bound recovers the single porosity response and the upper bound represents a realistic large value (Table 1).

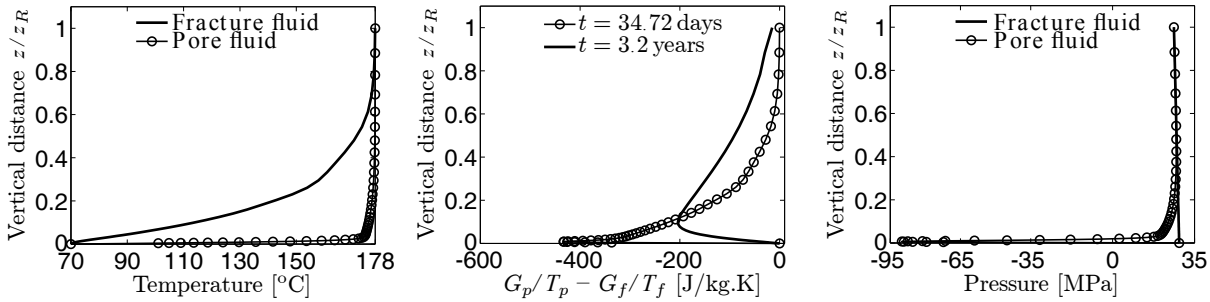

Figure 6: Fenton Hill reservoir, early time ($t = 34.72$ days) vertical profiles of fluid temperatures (left), and fluid pressures (right), and jump in scaled chemical potential at early and late times (middle). At early time, the temperature of the fracture fluid decreases, whereas the temperature of the pore fluid remains high. This large difference associated with a negative difference in scaled chemical potentials $G_p/T_p - G_f/T_f < 0$ induces a large transfer of mass from the fracture network towards the porous blocks, which is characterized by a significant pore pressure drop, while the fracture fluid pressure remains undisturbed as in Figure 4. This behavior matches the observations of field experiments, Murphy et al. [1981].

The material parameters matching field data for the Fenton Hill HDR reservoir are used, that is $k_f = 10^{-14}\,\mathrm{m}^2$ and $n^f = 0.005$. Again, the triple point of water is used as reference. The boundary conditions are detailed in Section 6.2. The vertical profiles of the temperatures and of the fluid pressures are plotted in Figure 7 for the late time $t = 3.17$ years. The effective stress and the strain responses are presented in Figures 8 and 9, respectively.

For small values of B, LTE between the solid phase and the fluid phases is enforced. Indeed, a small B represents a dense fracture network and reduces the spatial scale and the time scale separation between the porous blocks and the fracture network. Conversely, a large fracture spacing $B = 10\,\mathrm{m}$ reduces the specific surface area between the solid phase and the fracture fluid phase so that a LTNE model is required.

The fracture spacing B influences greatly the pore pressure response for the reasons explained earlier, whereas, the fracture fluid pressure remains undisturbed owing to its large permeability. It is worth noting that hydraulic equilibrium is not recovered unless thermal equilibrium is attained which *only* takes place for $B \to 0$ or at large times. This situation is due to the fact that the force driving mass transfer is a non-linear contribution in the form of a difference in scaled chemical potentials, $G_p/T_p - G_f/T_f$, between the pore fluid and the fracture fluid.

The change in effective stress results from the deformation and the solid temperature contributions. When both hydraulic and thermal equilibria are reached ($B \to 0$), the effective stress components become more tensile close to the injection area $z/z_R < 0.3$, the final state being more tensile than the initial state. An increase of fracture spacing B induces simultaneously (1) a departure from thermal equilibrium and thus a slower thermal depletion of the solid phase, and (2) a departure from hydraulic equilibrium and consequently a larger drop in pore pressure. These two contributions entail the change in effective stress by reducing (1) the rate of thermally induced stress and (2) the thermally induced tensile effective stress near the injection point.

The thermally induced contraction of the rock may have two adverse effects, a beneficial effect by increasing the aperture of fractures and a negative effect by increasing the aperture of the micro-fractures or pores. The first effect may favor the growth of the reservoir, whereas the second effect may favor fluid loss. The dual porosity model reveals that large fracture spacings B reduce significantly the thermally induced contraction of the rock in the vicinity of the injection well (Figure 9) and thereby the aforementioned effects, in particular the second negative effect. This observation advices against fracture clouds composed of many fractures with small spacings and argues in favor of multiple fracture systems with large fracture spacings, Tenzer [2001], Figure 2.

8.3. Influence of the reference thermodynamic potentials S^0 and G^0

The chemical potential (34) controls the rate of mass transfer (38). It is defined in terms of the reference thermodynamic potentials S^0 and G^0. A sensitivity analysis is proposed for two sets of reference thermodynamic potentials:

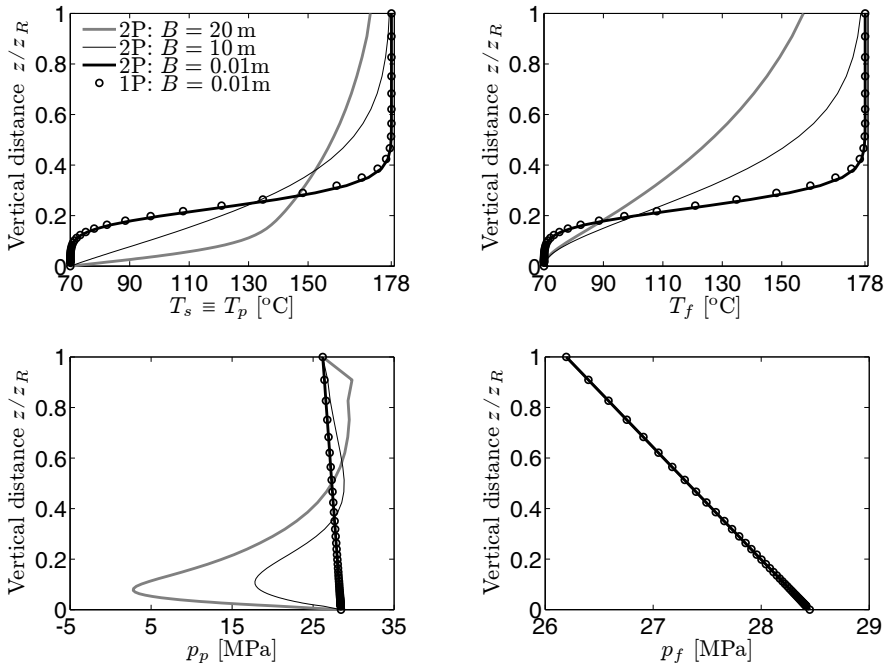

Figure 7: Fenton Hill reservoir, late time ($t = 3.17$ years) vertical profiles of solid and pore fluid temperatures (top-left), fracture fluid temperature (top-right), pore fluid pressure (bottom-left) and fracture fluid pressure (bottom-right) for $k_f = 10^{-14}\,\mathrm{m}^2$, $k_p = 10^{-20}\,\mathrm{m}^2$ and $n^f = 0.005$. A small fracture spacing B represents a dense fracture network that overlaps the response of the single porosity model, whereas a large B represents a sparsely fractured reservoir. The fracture spacing B controls the departure from *both* hydraulic and thermal equilibria. Hydraulic equilibrium is not recovered unless thermal equilibrium is attained, which takes place only for $B \to 0$. Solely, the fracture fluid pressure is not influenced by the fracture spacing B.

(1) for the first set, the injection state of the circulation test is used as reference: $S_{\mathrm{inj}} = 0.0$ and $G_{\mathrm{inj}} = 0.0$ for $T_{\mathrm{inj}} = 70\,^{\circ}\mathrm{C}$, $p_{\mathrm{inj}} = 27.44\,\mathrm{MPa}$;
(2) for the second set, the triple point of water is used as reference: $S_{\mathrm{TPW}} = 0.0$ and $G_{\mathrm{TPW}} = 0.0$ for $T_{\mathrm{TPW}} = 0.01\,^{\circ}\mathrm{C}$, $p_{\mathrm{TPW}} = 611.2\,\mathrm{Pa}$.

reference state	S^0 (kJ/K.kg)	G^0 (kJ/kg)
injection of the circulation test	1.136	-79.3
triple point of water	2.101	-187.6

Table 6: Two possible definitions of the reference thermodynamic potentials.

The ensuing thermodynamic potentials are listed in Table 6. The contours of the scaled chemical potential displayed in Figure 10 show a quantitative, rather than qualitative, influence of the reference potentials S^0 and G^0.

The tests of the previous subsection have been re-run, with the same material parameters, boundary conditions and initial conditions as detailed in Table 2. If the injection state of the circulation test is used as reference, mass transfer reduces in magnitude. However, the consequences on the various elements of the reservoir response, temperatures, pressures and stresses, are quite small at the late time $t = 3.17$ years as shown in Figure 11. Hence, the conclusions provided in subsections 8.1 and 8.2 are not affected.

8.4. Unconnected porosity

If the pore permeability tends to zero $k_p \to 0$, the response obtained with a single porosity model detailed in Appendix A should be recovered. This is the case if the porous block compressibility c_p is adequately estimated. c_p characterizes the intermediate stress-state of a loading decomposition problem, Khalili et

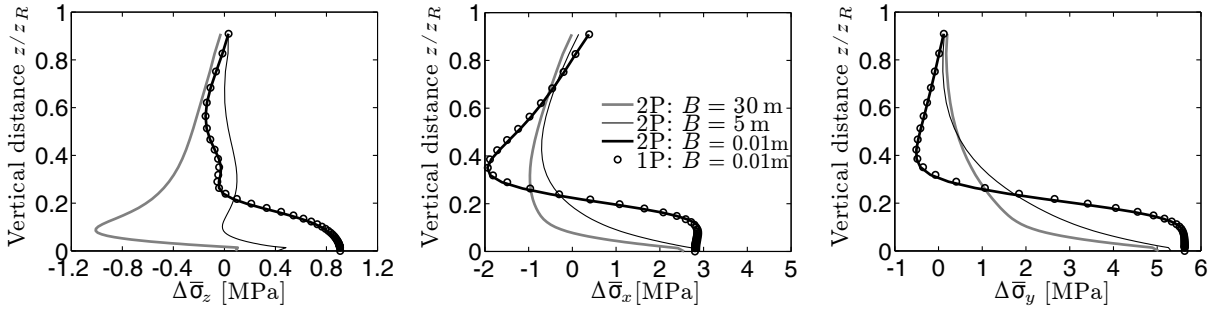

Figure 8: Fenton Hill reservoir, late time ($t = 3.17$ years) vertical profiles of the changes in vertical effective stress (left), in lateral effective stress (middle) and in out-of-plane effective stress (right) for $k_f = 10^{-14}\,\mathrm{m}^2$, $k_p = 10^{-20}\,\mathrm{m}^2$ and $n^f = 0.005$. For small fracture spacings $B \to 0$, hydraulic and thermal equilibria are reached and the changes in effective stress are tensile close to the injection area $z/z_R < 0.3$. In addition, the single porosity response is well recovered. The dual porosity model reveals that large fracture spacings B reduce the pore pressure and therefore the effective stress $\bar{\boldsymbol{\sigma}} = \boldsymbol{\sigma} + \xi_p\, p_p\, \mathbf{I} + \xi_f\, p_f \mathbf{I}$ is more compressive.

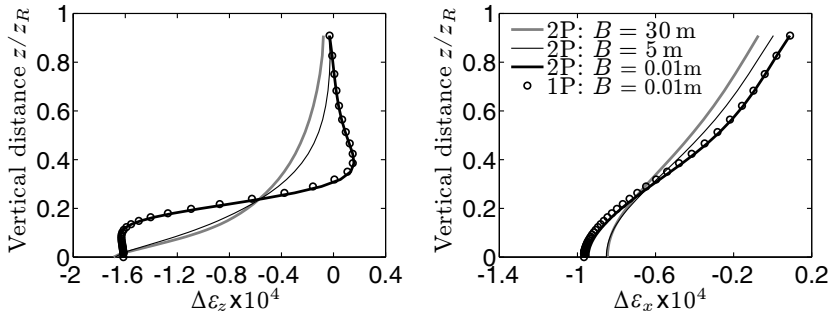

Figure 9: Fenton Hill reservoir, late time ($t = 3.17$ years) vertical profiles of the changes in vertical strain (left) and in lateral strain (right) with the same parameters as in Figure 8. For small fracture spacings $B \to 0$, hydraulic and thermal equilibria are reached and negative strains close to the injection area $z/z_R < 0.3$ characterize a sharp thermally induced contraction. In addition, the single porosity response is well recovered. The dual porosity model reveals that large fracture spacings B reduce the thermally induced contraction of the rock in the vicinity of the injection well and thereby the potential for aperture enlargement of the micro-fractures or pores.

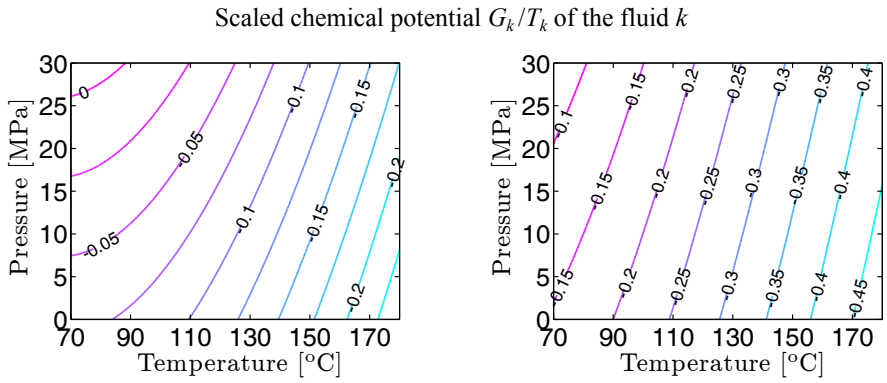

Figure 10: Scaled chemical potential [J/kg.K.10^3] as a function of temperature and pressure in a range appropriate to the present analysis. The material data are issued from Tables 2 and 4. (left): the injection state of the circulation test is taken as reference; (right): the triple point of water is taken as a reference.

al. [1996], which can be represented by the hydraulic characteristic time needed for the pore fluid to exit the porous block,

$$t_H = \frac{B^2}{4\alpha_H}, \quad \alpha_H = \frac{k_p}{\mu_p}\frac{2\mu^{\mathrm{DS}}(1-\nu)}{1-2\nu}\left[\frac{A^2(1+\nu_u)^2(1-2\nu)}{9(1-\nu_u)(\nu_u-\nu)}\right], \tag{69}$$

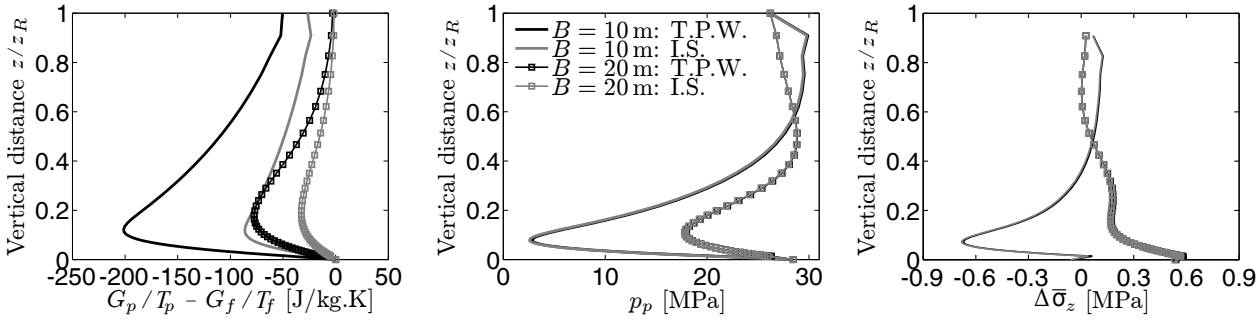

Figure 11: Fenton Hill reservoir, late time ($t = 3.17$ years) vertical profiles of jump in scaled chemical potentials (left), pore fluid pressure (middle), and change in vertical effective stress (right) for $k_f = 10^{-14}\,\mathrm{m}^2$, $k_p = 10^{-20}\,\mathrm{m}^2$ and $n^f = 0.005$. I.S. : the injection state of the circulation test is used as a reference. T.P.W. : the triple point of water is used as a reference. Mass transfer is larger for T.P.W. Although the pore pressure drop dissipates more effectively for larger mass transfer, the consequences on the reservoir response are quite small. For the pore fluid pressure and the change in vertical effective stress, the T.P.W. and the I.S. responses superpose.

in which α_H is the hydraulic diffusivity of the porous blocks, A is the Skempton coefficient and ν_u is the undrained Poisson's ratio,

$$\frac{1}{A} = 1 + n^f \frac{c_{p,H} - c_s}{c^{\mathrm{DS}} - c_s}, \quad \nu_u = \frac{3\nu + A(1-2\nu)(1 - c_s/c^{\mathrm{DS}})}{3 - A(1-2\nu)(1 - c_s/c^{\mathrm{DS}})}\,. \tag{70}$$

For geothermal reservoirs, the maximum time scale of the problem would be approximatively $t_{\max} \approx 30$ years, so that during the time span of interest, the porous block will remain undrained if $t_H > t_{\max}$ and $c_p = c_s$ should be enforced. The latter time constraint provides a bound to the permeability,

$$k_p < \frac{B^2}{4}\frac{\mu_p}{t_{\max}}\frac{1-2\nu}{2\mu^{\mathrm{DS}}(1-\nu)}\left[\frac{9(1-\nu_u)(\nu_u-\nu)}{A^2(1+\nu_u)^2(1-2\nu)}\right] \approx 2.3\times 10^{-23}\,\mathrm{m}^2 \tag{71}$$

below which a single porosity model can be safely used, i.e. the pore pressure influence can be disregarded. For higher permeabilities, the dual porosity model should be used to capture the correct stress evolution. It should be noted that for $t \approx t_H$, the pore pressure (induced by both early mass transfer and by thermal contraction) remains large and negative (Figure 12) which means that further fracturing cannot occur in the porous blocks and that any opening will be confined to the existing fractures. These aspects cannot be predicted using a single porosity model which will predict tensile stresses irrespective of the situation in the blocks.

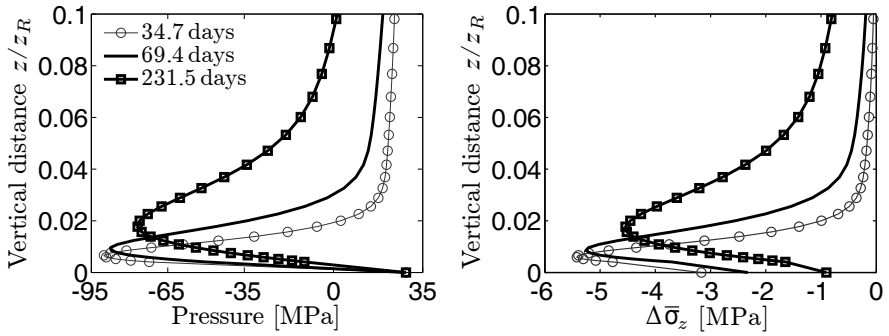

Figure 12: Fenton Hill reservoir close to the injection well $z/z_R \leq 0.1$, vertical profiles of pore pressure (left) and change in vertical effective stress (right) for $k_f = 10^{-14}\,\mathrm{m}^2$, $k_p = 10^{-21}\,\mathrm{m}^2$, $B = 13$ m and $n^f = 0.005$. The hydraulic characteristic time is $t_H \approx 50$ days. For times close to t_H, the pore pressure remains high and negative. However, for $t > t_H$ the excessive pore pressure can dissipate in the fracture network.

9. Conclusions

The main concern here has been to develop thermo-hydro-mechanical constitutive equations that exhibit key features of fractured media in local thermal non-equilibrium. A model describing the behavior of poro-elastic dual porous media has been extended to account for thermal contributions within a rational thermodynamics framework. The constitutive equations have been motivated and restricted by the Clausius-Duhem inequality to characterize the thermo-mechanical transfer and diffusion constitutive relations. Earlier poro-mechanical analyses, starting from Barenblatt et al. [1960], have considered the fluid transfer between the two cavities to be driven by the pressure jump. The extension to a mixture in local thermal non-equilibrium indicates that the driving engine for this mass transfer is the jump of the scaled chemical potential.

A finite element approximation has been developed that accounts for these constitutive features, and the thermo-hydro-mechanical couplings. The primary variables are the displacements, the pressures in the two cavities and the temperatures of the three phases. The non-linear field equations are solved using a full Newton-Raphson procedure. This finite element analysis has been employed to investigate the mechanisms of deformation, diffusion, forced convection and transfer in the context of heat extraction from a fractured hot dry rock reservoir.

Prior to the description of long term circulation tests, three parameters of the model have been calibrated with field data from two instrumented HDR reservoirs, namely from the Fenton Hill and Rosemanowes sites. Simulations highlight a local thermal non-equilibrium response characterized by three stages.

A sensitivity analysis has been carried out to study the influences of the dual porosity model and of the fracture spacing on the phase temperatures, the fluid pressures, and the effective stress. As expected, the dual porosity model provides, close to the injection well, a thermo-hydro-mechanical response which is bounded by the single porosity response and by the dual porosity response endowed with a low pore permeability. The drop in the thermally induced pore pressure is more pronounced when the fracture spacing is large. Hence, large fracture spacings tend to increase the compressive effective stress. In view of potential fluid loss due to the thermally induced rock contraction, the aforementioned effect advices against densely fractured reservoirs in favor of multiple fracture systems with large fracture spacings.

Accounting only for the fracture fluid and disregarding the pore pressure contribution, the single porosity approach overestimates the thermal contraction of fractured reservoirs. A dual porosity approach delivers information, (1) on fluid permeation in the porous matrix; (2) on the beneficial effect of the pore pressure contribution towards thermally induced stress; (3) on the history of the stress path and (4) on the optimum fracture spacing to reduce fluid loss induced by thermal contraction. Actually, the dual porosity response recovers well the field observations, e.g. Murphy et al. [1981], that fluid loss is high at the beginning of the circulation test and decreases with time.

Acknowledgments - This work is supported by a PhD fellowship from the French Ministry of Higher Education. RG would like to thank the Association Française des Femmes Diplomées des Universités (AFFDU) and the Institut National Polytechnique de Grenoble for their travel grants.

Appendix A. Reduction of the dual porosity model to a single porosity model

The dual porosity model reduces to a single porosity model by assuming that the volume fraction n^p of the pore fluid vanishes, which implies $c_p = c_s$. Consequently, the effective stress parameters reduce to,

$$\xi_p = 0, \quad \xi_f = 1 - \frac{c_s}{c^{\mathrm{DS}}}\,. \tag{A.1}$$

Hence, the field equations (43) to (49) describe the balance of momentum of the mixture, the balance of mass of the fracture fluid, and the balances of energy of the solid and of the fracture fluid, namely,

$$\mu^{\mathrm{DS}}\,\nabla^2\mathbf{u} + (\lambda^{\mathrm{DS}} + \mu^{\mathrm{DS}})\,\nabla(\mathrm{div}\,\mathbf{u}) - \xi_f\,\nabla p_f - \frac{c_T}{c^{\mathrm{DS}}}\,\nabla T_s = \mathbf{0}\,, \tag{A.2}$$

$$\mathrm{div}\left(\frac{k_f}{\mu_f}\,\nabla p_f + n^f\,\Theta_f\,\nabla T_f\right) = a_{ff}\frac{\partial p_f}{\partial t} + \xi_f\,\mathrm{div}\,\frac{\partial \mathbf{u}}{\partial t} + a_{fT_s}\frac{\partial T_s}{\partial t} + a_{fT_f}\frac{\partial T_f}{\partial t}\,, \tag{A.3}$$

$$\text{div}\ (n^s \Lambda_s\, \nabla T_s) = a_{T_s T_s} \frac{\partial T_s}{\partial t} + T_s \frac{c_T}{c^{\text{DS}}}\, \text{div}\, \frac{\partial \mathbf{u}}{\partial t} + T_s\, a_{f T_s} \frac{\partial p_f}{\partial t} + \kappa_{sf}\, (T_s - T_f)\ , \tag{A.4}$$

$$\text{div}\ \left(n^f \Lambda_f\, \nabla T_f + T_f n^f \Theta_f\, \nabla p_f\right) = a_{T_f T_f} \frac{\partial T_f}{\partial t} + T_f\, a_{f T_f} \frac{\partial p_f}{\partial t} + \mathbf{M}_f \cdot \nabla\, H_f + \kappa_{sf}\, (T_f - T_s)\ , \tag{A.5}$$

while the balance of mass and the balance of energy of the pore fluid become elusive.

Appendix B. Definition of the element matrices $\mathbb{K}^e$ and $\mathbb{D}^e$

The submatrices of the element generalized stiffness-convection matrix (62) are built from the constitutive matrices, namely

$$\mathbf{K}^e_{\mathbf{u}\mathbf{u}} = \mathbf{E}^e_{\mathbf{u}\mathbf{u}}, \quad \mathbf{K}^e_{\mathbf{u}p_p} = -\xi_p\, \mathbf{C}^e_{\mathbf{u}p}, \quad \mathbf{K}^e_{\mathbf{u}p_f} = -\xi_f\, \mathbf{C}^e_{\mathbf{u}p}, \quad \mathbf{K}^e_{\mathbf{u}T_s} = -c_T/c^{\text{DS}}\, \mathbf{C}^e_{\mathbf{u}T}; \tag{B.1}$$

$$\mathbf{K}^e_{p_p p_p} = -\mathbf{J}^e_{k_p} - \gamma_{pp}\, \mathbf{M}^e_{pp},\ \mathbf{K}^e_{p_p p_f} = \gamma_{pp}\, \mathbf{M}^e_{pp},\ \mathbf{K}^e_{p_p T_p} = -\mathbf{J}^e_{\Theta_p} - \gamma_{pT}\, \mathbf{M}^e_{pT},\ \mathbf{K}^e_{p_p T_f} = \gamma_{pT}\, \mathbf{M}^e_{pT}; \tag{B.2}$$

$$\mathbf{K}^e_{p_f p_f} = -\mathbf{J}^e_{k_f} - \gamma_{pp}\, \mathbf{M}^e_{pp},\ \mathbf{K}^e_{p_f p_p} = \gamma_{pp}\, \mathbf{M}^e_{pp},\ \mathbf{K}^e_{p_f T_f} = -\mathbf{J}^e_{\Theta_f} - \gamma_{pT}\, \mathbf{M}^e_{pT},\ \mathbf{K}^e_{p_f T_p} = \gamma_{pT}\, \mathbf{M}^e_{pT}; \tag{B.3}$$

$$\mathbf{K}^e_{T_s T_s} = -\mathbf{Q}^e_{\Lambda_s} - (\kappa_{sp} + \kappa_{sf})\, \mathbf{M}^e_{TT}, \quad \mathbf{K}^e_{T_s T_p} = \kappa_{sp}\, \mathbf{M}^e_{TT}, \quad \mathbf{K}^e_{T_s T_f} = \kappa_{sf}\, \mathbf{M}^e_{TT}; \tag{B.4}$$

$$\begin{aligned}
&\mathbf{K}^e_{T_p p_p} = -\mathbf{Q}^e_{\Theta_p} - \gamma_{T_p p}\, (\mathbf{M}^e_{pT})^{\mathrm{T}} - b_{T_p p}\, \mathbf{C}^e_{Tp,\mathrm{v}_p},\\
&\mathbf{K}^e_{T_p p_f} = \gamma_{T_p p}\, (\mathbf{M}^e_{pT})^{\mathrm{T}},\\
&\mathbf{K}^e_{T_p T_s} = \kappa_{sp}\, \mathbf{M}^e_{TT},\\
&\mathbf{K}^e_{T_p T_p} = -\mathbf{Q}^e_{\Lambda_p} - (\kappa_{sp} + \kappa_{pf} + \gamma_{T_p T_p})\, \mathbf{M}^e_{TT} - b_{T_p T_p}\, \mathbf{C}^e_{TT,\mathrm{v}_p},\\
&\mathbf{K}^e_{T_p T_f} = (\kappa_{pf} + \gamma_{T_p T_p})\, \mathbf{M}^e_{TT};
\end{aligned} \tag{B.5}$$

$$\begin{aligned}
&\mathbf{K}^e_{T_f p_p} = -\gamma_{T_f f}\, (\mathbf{M}^e_{pT})^{\mathrm{T}},\\
&\mathbf{K}^e_{T_f p_f} = -\mathbf{Q}^e_{\Theta_f} + \gamma_{T_f f}\, (\mathbf{M}^e_{pT})^{\mathrm{T}} - b_{T_f f}\, \mathbf{C}^e_{Tp,\mathrm{v}_f},\\
&\mathbf{K}^e_{T_f T_s} = \kappa_{sf}\, \mathbf{M}^e_{TT}\\
&\mathbf{K}^e_{T_f T_p} = (\kappa_{pf} - \gamma_{T_f T_f})\, \mathbf{M}^e_{TT},\\
&\mathbf{K}^e_{T_f T_f} = -\mathbf{Q}^e_{\Lambda_f} - (\kappa_{sf} + \kappa_{pf} - \gamma_{T_f T_f})\, \mathbf{M}^e_{TT} - b_{T_f T_f}\, \mathbf{C}^e_{TT,\mathrm{v}_f},
\end{aligned} \tag{B.6}$$

in which the coefficients have been linearized around the reference configuration,

$$\begin{aligned}
&\gamma_{pp} = \eta, \quad \gamma_{pT} = -\eta\, \rho_p\, S^0\,,\\
&\gamma_{T_p p} = +\eta\, \rho_p \times (C^{(p)}_p T^0 - H^0), \quad \gamma_{T_p T_p} = -\eta\, \rho_p^2\, S^0 \times (C^{(p)}_p T^0 - H^0)\,,\\
&\gamma_{T_f f} = -\eta\, \rho_p \times (C^{(p)}_f T^0 - H^0)\,, \quad \gamma_{T_f T_f} = +\eta\, \rho_p^2\, S^0 \times (C^{(p)}_f T^0 - H^0)\,,\\
&b_{T_p p} = n^p\, (1 - c_{pT}\, T^0), \quad b_{T_f f} = n^f\, (1 - c_{fT}\, T^0),\\
&b_{T_p T_p} = n^p\, \rho_p\, C^{(p)}_p, \quad b_{T_f T_f} = n^f \rho_f\, C^{(p)}_f\,.
\end{aligned} \tag{B.7}$$

The submatrices of the generalized diffusion matrix (61),

$$\begin{aligned}
&\mathbf{D}^e_{p_p \mathbf{u}} = -\xi_p \mathbf{C}^e_{p\mathbf{u}}, \qquad \mathbf{D}^e_{p_p p_p} = -a_{pp} \mathbf{M}^e_{pp},\\
&\mathbf{D}^e_{p_p p_f} = -a_{pf} \mathbf{M}^e_{pp}, \quad \mathbf{D}^e_{p_p T_s} = -a_{pT_s} \mathbf{M}^e_{pT}, \quad \mathbf{D}^e_{p_p T_p} = -a_{pT_p} \mathbf{M}^e_{pT};
\end{aligned} \tag{B.8}$$

$$\begin{aligned}
&\mathbf{D}^e_{p_f \mathbf{u}} = -\xi_f \mathbf{C}^e_{p\mathbf{u}}, \qquad \mathbf{D}^e_{p_f p_p} = -a_{pf} \mathbf{M}^e_{pp},\\
&\mathbf{D}^e_{p_f p_f} = -a_{ff} \mathbf{M}^e_{pp}, \quad \mathbf{D}^e_{p_f T_s} = -a_{fT_s} \mathbf{M}^e_{pT}, \quad \mathbf{D}^e_{p_f T_f} = -a_{fT_f} \mathbf{M}^e_{pT};
\end{aligned} \tag{B.9}$$

$$\begin{aligned}
&\mathbf{D}^e_{T_s\mathbf{u}} = -T_s\, c_T/c^{\mathrm{DS}}\ \mathbf{C}^e_{T\mathbf{u}}, \quad \mathbf{D}^e_{T_sp_p} = -T_s a_{pT_s}(\mathbf{M}^e_{pT})^{\mathrm{T}},\\
&\mathbf{D}^e_{T_sp_f} = -T_s a_{fT_s}(\mathbf{M}^e_{pT})^{\mathrm{T}}, \quad \mathbf{D}^e_{T_sT_s} = -a_{T_sT_s}\mathbf{M}^e_{TT};
\end{aligned} \tag{B.10}$$

$$\mathbf{D}^e_{T_pp_p} = -T_p a_{pT_p}(\mathbf{M}^e_{pT})^{\mathrm{T}}, \quad \mathbf{D}^e_{T_pT_p} = -a_{T_pT_p}\mathbf{M}^e_{TT}; \tag{B.11}$$

$$\mathbf{D}^e_{T_fp_f} = -T_f a_{fT_f}(\mathbf{M}^e_{pT})^{\mathrm{T}}, \quad \mathbf{D}^e_{T_fT_f} = -a_{T_fT_f}\mathbf{M}^e_{TT}\,, \tag{B.12}$$

involve coefficients defined in (50).

The finite element sub-matrices of the weak formulation in equations (B.1) to (B.12) are listed below, starting with the [1×4] vectors of shape functions,

$$\mathbf{N}_p \;=\; \mathbf{N}_T \;=\; \left[\begin{array}{cccc} N^1 & N^2 & N^3 & N^4 \end{array}\right], \tag{B.13}$$

which are identical for the pressure and temperature fields. N^1, N^2, N^3 and N^4 are the shape functions of the Q4 elements. $\mathbf{N}_\mathbf{u}$ is the expanded shape function vector of size [2×8] for the displacement.

Five matrices are involved in the balance of momentum of the mixture,

$$\begin{aligned}
\mathbf{E}^e_{\mathbf{uu}} &= \int_{V^e} (\mathbf{B}_\mathbf{u})^{\mathrm{T}}\, \mathbf{D}_{\mathrm{el}}\, \mathbf{B}_\mathbf{u}\ dV^e,\\
\mathbf{C}^e_{\mathbf{u}p} &= \int_{V^e} (\nabla\mathbf{N}_\mathbf{u})^{\mathrm{T}}\, \mathbf{N}_p\ dV^e, \qquad \mathbf{C}^e_{\mathbf{u}T} = \int_{V^e} (\nabla\mathbf{N}_\mathbf{u})^{\mathrm{T}}\, \mathbf{N}_T\ dV^e.\\
\mathbf{C}^e_{p\mathbf{u}} &= \int_{V^e} (\mathbf{N}_p)^{\mathrm{T}}\ [1\ \ 1]\ \nabla\cdot\mathbf{N}_\mathbf{u}\ dV^e, \qquad \mathbf{C}^e_{T\mathbf{u}} = \int_{V^e} (\mathbf{N}_T)^{\mathrm{T}}\,[1\ \ 1]\ \ \nabla\cdot\mathbf{N}_\mathbf{u}\, dV^e.
\end{aligned} \tag{B.14}$$

where $\mathbf{D}_{\mathrm{el}}$ is the drained stiffness matrix and $\mathbf{B}_\mathbf{u}$ is the strain displacement matrix. The next matrices pertain to hydraulic conductivity and heat conduction,

$$\begin{aligned}
\mathbf{J}^e_{k_p} &= \int_{V^e} (\nabla\mathbf{N}_p)^{\mathrm{T}}\, \frac{k_p}{\mu_p}\, \nabla\mathbf{N}_p\ dV^e, \qquad \mathbf{J}^e_{k_f} = \int_{V^e} (\nabla\mathbf{N}_p)^{\mathrm{T}}\, \frac{k_f}{\mu_f}\, \nabla\mathbf{N}_p\ dV^e,\\
\mathbf{Q}^e_{\Lambda_s} &= \int_{V^e} (\nabla\mathbf{N}_T)^{\mathrm{T}}\, n^s\, \Lambda_s\, \nabla\mathbf{N}_T\ dV^e, \qquad \mathbf{Q}^e_{\Lambda_p} = \int_{V^e} (\nabla\mathbf{N}_T)^{\mathrm{T}}\, n^p\, \Lambda_p\, \nabla\mathbf{N}_T\ dV^e,\\
\mathbf{Q}^e_{\Lambda_f} &= \int_{V^e} (\nabla\mathbf{N}_T)^{\mathrm{T}}\, n^f\, \Lambda_f\, \nabla\mathbf{N}_T\ dV^e\,,
\end{aligned} \tag{B.15}$$

while the matrices below are involved in the thermo-osmosis and coupled isothermal heat flow,

$$\begin{aligned}
\mathbf{J}^e_{\Theta_p} &= \int_{V^e} (\nabla\mathbf{N}_p)^{\mathrm{T}}\, n^p\, \Theta_p\, \nabla\mathbf{N}_T\ dV^e, \qquad \mathbf{J}^e_{\Theta_f} = \int_{V^e} (\nabla\mathbf{N}_p)^{\mathrm{T}}\, n^f\, \Theta_f\, \nabla\mathbf{N}_T\ dV^e,\\
\mathbf{Q}^e_{\Theta_p} &= \int_{V^e} (\nabla\mathbf{N}_T)^{\mathrm{T}}\, T_p n^p\, \Theta_p\, \nabla\mathbf{N}_p\ dV^e, \qquad \mathbf{Q}^e_{\Theta_f} = \int_{V^e} (\nabla\mathbf{N}_T)^{\mathrm{T}}\, T_f n^f\, \Theta_f\, \nabla\mathbf{N}_p\ dV^e\,.
\end{aligned} \tag{B.16}$$

Three mass matrices are required in the general case,

$$\begin{aligned}
\mathbf{M}^e_{pp} &= \int_{V^e} (\mathbf{N}_p)^{\mathrm{T}}\, \mathbf{N}_p\ dV^e, \qquad \mathbf{M}^e_{TT} = \int_{V^e} (\mathbf{N}_T)^{\mathrm{T}}\, \mathbf{N}_T\ dV^e,\\
\mathbf{M}^e_{pT} &= \int_{V^e} (\mathbf{N}_p)^{\mathrm{T}}\, \mathbf{N}_T\ dV^e\,.
\end{aligned} \tag{B.17}$$

Note that they actually reduce to a single matrix if the same shape function is used for the pressures and the temperatures, namely $\mathbf{N}_p = \mathbf{N}_T$.

The four convective matrices discretised with the Galerkin method adopt the format,

$$\begin{aligned}
\mathbf{C}^e_{TT,\mathrm{v}_p} &= \int_{V^e} (\mathbf{N}_T)^{\mathrm{T}}\, (\mathbf{v}_p - \mathbf{v}_s)\cdot\nabla\mathbf{N}_T\ dV^e, \quad \mathbf{C}^e_{Tp,\mathrm{v}_p} = \int_{V^e} (\mathbf{N}_T)^{\mathrm{T}}\, (\mathbf{v}_p - \mathbf{v}_s)\cdot\nabla\mathbf{N}_p\ dV^e,\\
\mathbf{C}^e_{TT,\mathrm{v}_f} &= \int_{V^e} (\mathbf{N}_T)^{\mathrm{T}}\, (\mathbf{v}_f - \mathbf{v}_s)\cdot\nabla\mathbf{N}_T\ dV^e, \quad \mathbf{C}^e_{Tp,\mathrm{v}_f} = \int_{V^e} (\mathbf{N}_T)^{\mathrm{T}}\, (\mathbf{v}_f - \mathbf{v}_s)\cdot\nabla\mathbf{N}_p\ dV^e.
\end{aligned} \tag{B.18}$$

[1] E.C. Aifantis, 1980a. On the problem of diffusion in solids, Acta Mechanica, 37, 265-296.

[2] E.C. Aifantis, 1980b. Further comments on the problem of heat extraction from hot dry rocks, Mechanics Research Communications, 7, 219-226.

[3] H.C.H. Armstead and J.W. Tester, 1987. Heat mining, E.&F.N. Spon Ltd., London and New York.

[4] M. Bai and J.C. Rogiers, 1994. Fluid Flow and Heat Flow in deformable Fractured Porous Media, International Journal of Engineering Science, 32, 1615-1633.

[5] G.I. Barenblatt, U.P. Zheltov and G.H. Kochina, 1960. Basic Concepts in the Theory of Seepage of Homogeneous Liquids in Fissured Rocks, Journal of Applied Mathematics and Mechanics, English Translation, 24, 1286-1303.

[6] A. Bataillé, P. Genthon, M. Rabinowicz and B. Fritz, 2006. Modeling the coupling between free and forced convection in a vertical permeable slot: implications for the heat production of an Enhanced Geothermal System, Geothermics, 35, 654-682.

[7] A. Bejan, 1993. Heat Transfer, John Wiley & Sons Inc..

[8] T. Belytschko and T.J.R. Hughes, 1983. Computational methods for transient analysis, North-Holland, Computational Methods in Mechanics, Amsterdam.

[9] M.A. Biot, 1941. General theory of three-dimensional consolidation, Journal of Applied Physics, 12, 155-164.

[10] M.A. Biot, 1977. Variational-lagrangian thermodynamics of nonisothermal finite strain mechanics of porous solids and thermomolecular diffusion, International Journal of Solids and Structures, 13(6), 579-597.

[11] R.M. Bowen and P.J. Chen, 1975. Waves in a binary mixture of linear elastic materials, Journal de Mécanique, 14, 237-266.

[12] R.M. Bowen and D.J. Garcia, 1970. On the thermodynamics of mixtures with several temperatures, International Journal of Engineering Science, 8, 63-83.

[13] K.M. Bower and G. Zyvoloski, 1997. A numerical model for thermo-hydro-mechanical coupling in fractured rock, International Journal of Rock Mechanics and Mining Sciences, 34, 1201-1211.

[14] D. Brown, R. DuTeaux, P. Kruger, D. Swenson and T. Yamaguchi, 1999. Fluid circulation and heat extraction from engineered geothermal reservoirs, Geothermics, 28, 553-572.

[15] D. Bruel, 1995. Heat extraction modelling from forced fluid flow through stimulated fractured rock masses: application to the Rosemanowes hot dry rock reservoir, Geothermics, 24, 361-374.

[16] D. Bruel, 2002. Impact of Induced Thermal Stresses During Circulation Tests in an Engineered Fractured Geothermal Reservoir: Example of the Soultz-Sous-Forêts European Hot Fractured Rock Geothermal Project, Rhine Graben, France, Oil & Gas Science and Technology, 57, 459-470.

[17] V. De La Cruz and T.J.T. Spanos, 1989. Thermomechanical coupling during seismic wave propagation in a porous medium, Journal of Geophysical Research, 94, 637-642.

[18] G. de Marsily, 1981. Quantitative Hydrogeology - Groundwater Hydrology for Engineers, Academic Press, Masson, Paris.

[19] R. DuTeaux, D. Swenson and B. Hardeman, 1996. Insight from modelling discrete fractures using GEOCRACK, Proceedings, Twenty-First Workshop on Geothermal Reservoir Engineering, Stanford University, Stanford, California,

[20] D. Elsworth, 1989. Theory of Thermal Recovery From a Spherically Stimulated Hot Dry Rock Reservoir, Journal of Geophysical Research, 94, 1927-1934.

[21] D. Elsworth and M. Bai, 1992. Flow-deformation response of dual-porosity media, Journal of Geotechnical Engineering, 118, 107-124.

[22] A.C. Eringen and J.D. Ingram, 1965. A continuum theory of chemically reacting media, International Journal of Engineering Science, 3, 197-212.

[23] R. Gelet, 2011. Thermo-hydro-mechanical study of deformable porous media with double porosity in local thermal non-equilibrium, PhD thesis, Institut National Polytechnique de Grenoble, France, and The University of New South Wales, Sydney, Australia.

[24] R. Gelet, B. Loret and N. Khalili, 2011. Borehole Stability Analysis in a Thermo-Poro-Elastic Dual Porosity Medium, Accepted for publication, International Journal of Rock Mechanics and Mining Sciences & Geomechanics Abstracts.

[25] R. Gelet, B. Loret and N. Khalili, 2012. Thermal recovery from a fractured medium in local thermal non-equilibrium, Submitted for publication.

[26] A. Ghassemi, S. Tarasovs and A.H.-D. Cheng, 2005. Integral equation solution of heat extraction-induced thermal stress in enhanced geothermal reservoirs, International Journal for Numerical and Analytical Methods in Geomechanics, 29, 829-844.

[27] A. Ghassemi, A. Nygren and A. Cheng, 2008. Effects of heat extraction on fracture aperture: A poro-thermoelastic analysis, Geothermics, 37, 525-539.

[28] K. Hayashi, J. Willis-Richards, R.J. Hopkirk and Y. Niibori, 1999. Numerical models of HDR geothermal reservoirs–a review of current thinking and progress, Geothermics, 28, 507-518.

[29] T.W. Hicks, R.J. Pine, J. Willis-Richards, S. Xu, A.J. Jupe and N.E.V. Rodrigues, 1996. A hydro-thermo-mechanical numerical model for HDR geothermal reservoir evaluation, International Journal of Rock Mechanics and Mining Sciences & Geomechanics Abstracts, 33(5), 499-511.

[30] C.T. Hsu, 1999. A closure model for transient heat conduction in porous media, Journal of Heat Transfer, 121, 733-739.

[31] T.J.R. Hughes, 1987. The Finite Element Method. Linear Static and Dynamic Finite Element Analysis, Prentice-Hall, Englewood Cliffs, NJ.

[32] P.X. Jiang, R.N. Xu and W. Gong, 2006. Particle-to-fluid heat transfer coefficients in miniporous media, Chemical Engineering Science, 61, 7213-7222.

[33] H. Kazemi, 1969. Pressure Transient Analysis of Naturally Fractured Reservoirs with Uniform Fracture Distribution, Society of Petroleum Engineers Journal, 9(4), 451-462.

[34] J. Kestin, 1966. A Course in Thermodynamics, vol. I, Blaisdell Publishing Co., Waltham, Massachusetts.

[35] N. Khalili and A.P.S. Selvadurai, 2003. A Fully Coupled Constitutive Model for Thermo-Hydro-Mechanical Analysis in elastic media with double porosity, Geophysical Research Letters, 30(24), 1-5.

[36] N. Khalili and B. Loret, 2001. An Elasto-plastic Model for Non-Isothermal Analysis of Flow and Deformation in Unsaturated Porous Media Formulation, International Journal of Solids and Structures, 38, 8305-8330.

[37] N. Khalili and S. Valliappan, 1996. Unified Theory of Flow and Deformation in double porous media, European Journal of Mechanics - A/Solids, 15(2), 321-336.

[38] T. Kohl, K.F. Evansi, R.J. Hopkirk and L. Rybach, 1995. Coupled hydraulic, thermal and mechanical considerations for the simulation of hot dry rock reservoirs, Geothermics, 24, 345-359.

[39] O. Kolditz and C. Clauser, 1998. Numerical simulation of flow and heat transfer in fractured crystalline rocks: Application to the hot dry rock site in Rosemanowes (U.K.), Geothermics, 27, 1-23.

[40] B. Loret, 2008. Biomechanical aspects of soft tissues, unpublished lecture notes.

[41] B. Loret and N. Khalili, 2000a. Thermo-mechanical potentials for unsaturated Soils, CISM Courses and Lectures 426 "Advanced Numerical Applications and Plasticity in Geomechanics", Udine, Italy; edited by D.V. Griffiths and G. Gioda, Springer Wien New York (2001), 253-276.

[42] B. Loret and N. Khalili, 2000b. A three-phase model for unsaturated soils, International Journal for Numerical and Analytical Methods in Geomechanics, 24, 893-927.

[43] I. Masters, W.K.S. Pao and R.W. Lewis, 2000. Coupling Temperature to a Double-porosity model of deformable porous media, International Journal for Numerical Methods in Engineering, 49, 421-438.

[44] W.J. Minkowycz, A. Haji-Sheikh and K. Vafai, 1999. On departure from local thermal equilibrium in porous media due to a rapidly changing heat source: the Sparrow number, International Journal of Heat and Mass Transfer, 42, 3373-3385.

[45] J.K. Mitchell, 1993. Fundamentals of Soil Behavior, J. Wiley & Sons, New York.

[46] H.D. Murphy, R.G. Lawton, J.W. Tester, R.M. Potter, D.W. Brow and R.L. Aamodt, 1977. Preliminary assessment of a geothermal energy reservoir formed by hydraulic fracturing, Society of Petroleum Engineers Journal, 17, 317-326.

[47] H.D. Murphy, J.W. Tester, C.O. Grigsby and R.M. Potter, 1981. Energy extraction from fractured geothermal reservoirs in low-permeability crystalline rock, Journal of Geophysical Research, 86, 7145-7158.

[48] R. Nair, Y. Abousleiman and M. Zaman, 2004. A finite element porothermoelastic model for dual-porosity media, International Journal for Numerical and Analytical Methods in Geomechanics, 28, 875-898.

[49] D.A. Nield, A.V. Kuznetsov and M. Xiong, 2002. Effect of local thermal non-equilibrium on thermally developing forced convection in a porous medium, International Journal of Heat and Mass Transfer, 45, 4949-4955.

[50] C. Pecker and H. Deresiewicz, 1973. Thermal effects on wave propagation in liquid-filled porous media, Acta Mechanica, 16, 45-64.

[51] H.G. Richards, R.H. Parker, A.S.P. Green, R.H. Jones, J.D.M. Nicholls, D.A.C. Nicol, M.M. Randall, S. Richards, R.C. Stewart and J. Willis-Richards, 1994. The performance and characteristics of the experimental hot dry rock geothermal reservoir at Rosemanowes, Cornwall (1985-1988), Geothermics, 23(2), 73-109.

[52] N. Tenma, T. Yamaguchi and G. Zyvoloski, 2008. The Hijiori Hot Dry Rock test site, Japan: Evaluation and optimization of heat extraction from a two-layered reservoir, Geothermics, 37, 19-52.

[53] H. Tenzer, 2001. Development of hot dry rock technology, Bulletin Geo-Heat Center, 32, 14-22.

[54] N. Wakao and S. Kaguei, 1982. Heat and Mass Transfer in Packed Beds, Gordon and Breach, Science Publishers, New York.

[55] J.B. Warren and P.J. Root, 1963. The Behaviour of Naturally Fractured Reservoirs, Society of Petroleum Engineers Journal, 3, 245-255.

[56] R.K. Wilson and E.C. Aifantis, 1982. On the theory of consolidation with double porosity, International Journal of Engineering Science, 20(9), 1009-1035.

[57] F. Zanotti and R.G. Carbonell, 1984. Development of Transport Equations for Multiphase Systems, I-II-III, Chemical Engineering Science, 39, 263-278, 279-297, 299-311.

[58] J. Zhang and J.C. Roegiers, 2005. Double Porosity Finite Element Method for Borehole Modeling, Rock Mechanics and Rock Engineering, 38, 217-242.

[59] G.A. Zyvoloski, R.L. Aamodt and R.G. Aguilar, 1981. Evaluation of the second hot dry rock geothermal energy reservoir: results of Phase I, Run Segment 5, Report LA-8940-HDR, Los Alamos National Laboratory, NM (USA).